

Optimization of 1-D Unidirectional Leaky-Wave Antennas Based on Partially Reflecting Surfaces

Walter Fuscaldo¹, Senior Member, IEEE, Alessandro Galli², Member, IEEE,
and David R. Jackson³, Fellow, IEEE

Abstract—In a previous work, we derived optimum conditions for the design of finite-size 1-D unidirectional leaky-wave antennas (LWAs) in the general case. The bandwidth and the gain–bandwidth figure of merit are, however, structure-specific and have not been discussed yet. A practical case that is widely investigated in the literature is that of 1-D unidirectional LWAs based on partially reflecting surfaces (PRSs). In this work, we not only evaluate these features for this specific class of antennas, but we also derive design rules for optimizing the PRS impedance and cavity height to get maximum gain. Numerical results and full-wave simulations are finally proposed for a realistic example based on a metal strip-grating structure, to validate the theoretical findings.

Index Terms—Bandwidth, gain, leaky-wave antennas, leaky waves, partially reflecting surfaces, radiation patterns.

I. INTRODUCTION

MANY modern antenna applications require low-cost solutions capable of providing high directivity with low fabrication complexity. In this context, leaky-wave antennas (LWAs) have so far represented a reference solution in the microwave frequency range [1], [2], and more recently in the optical [3] and terahertz (THz) regimes [4]. In particular, unidirectional 1-D LWAs provide a simple means to achieve a highly directive beam with a continuous beamscanning over frequency. These features are of great interest at microwaves for 5G applications where spatial frequency multiplexing [5] is required, and for optical and THz applications [3], [6], where the design of highly directive antennas with controlled beam radiation still represents a challenging task.

In previous work [7], we derived conditions for minimizing the beamwidth or maximizing the gain of finite-size 1-D unidirectional LWAs. In order to evaluate the gain with a fully analytical procedure, a “correction function” has been

Manuscript received 25 October 2021; revised 4 March 2022; accepted 5 April 2022. Date of publication 30 May 2022; date of current version 6 October 2022. (Corresponding author: Walter Fuscaldo.)

Walter Fuscaldo is with the Consiglio Nazionale delle Ricerche, Istituto per la Microelettronica e Microsistemi, 00133 Rome, Italy (e-mail: walter.fuscaldo@cnr.it).

Alessandro Galli is with the Department of Information Engineering, Electronics and Telecommunications, Sapienza University of Rome, 00184 Rome, Italy (e-mail: alessandro.galli@uniroma1.it).

David R. Jackson is with the Department of Electrical and Computer Engineering, University of Houston, Houston, TX 77204 USA (e-mail: djackson@uh.edu).

Color versions of one or more figures in this article are available at <https://doi.org/10.1109/TAP.2022.3177568>.

Digital Object Identifier 10.1109/TAP.2022.3177568

0018-926X © 2022 IEEE. Personal use is permitted, but republication/redistribution requires IEEE permission.
See <https://www.ieee.org/publications/rights/index.html> for more information.

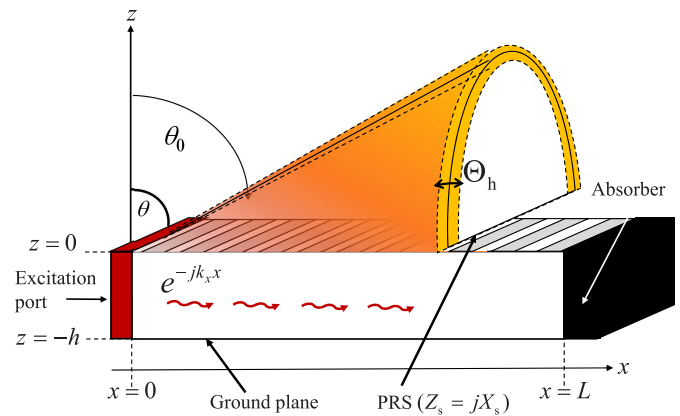


Fig. 1. Schematic representation of a PRS-based 1-D unidirectional LWA radiating a conical beam at θ_0 (θ being the elevation angle of observation). The PRS is represented with a single scalar sheet impedance Z_s .

defined, which allows for accurately estimating the gain from the knowledge of the beamwidth.

In [7], the normalized phase $\hat{\beta} = \beta/k_0$ and attenuation $\hat{\alpha} = \alpha/k_0$ constants ($k_0 = 2\pi/\lambda_0$ and λ_0 being the free-space wavenumber and wavelength, respectively) are varied *freely*; thus, the optimization procedure applies, in principle, to any 1-D unidirectional LWA. However, for the general case discussed there, it was not possible to determine either the bandwidth performance or the gain–bandwidth figure of merit (FoM) as these features are structure-specific.

A practical example that we discuss here is that of 1-D unidirectional LWAs based on a partially reflecting surface (PRS) (see Fig. 1). Examples of such antennas include (but are not limited to) substrate–superstrate LWAs [8], multi-layered LWAs [9], and metasurface LWAs [4], as all these types of antennas can be interpreted through the PRS concept (e.g., [10]–[12] for a rigorous analysis). In practice, most uniform and quasi-uniform LWAs [1] allow for a PRS interpretation, thus making the results of this work applicable to a broad extent.

Another relevant advantage of the PRS concept is the existence of an approximate analytical expression for the frequency dispersion of the leaky wavenumber which does not depend on the TE/TM nature of the leaky wavenumber nor on the inductive/capacitive character of the PRS (however, the PRS has to be highly reflective for these relations to hold true). As a result, it is possible to derive simple analytical formulas for determining the bandwidth performance and the

gain–bandwidth FoM. It is worthwhile to stress here that the bandwidth performance of a PRS-based 1-D unidirectional LWA considerably differs from that of PRS-based 1-D bidirectional LWAs or 2-D LWAs, which have been investigated in the literature with specific reference to broadside radiation [13]–[21]. This is definitely not the case for 1-D unidirectional LWAs that usually radiate far from broadside, and for which an accurate bandwidth analysis was so far lacking. Interestingly, we demonstrate here that the gain–bandwidth FoM decreases slightly with the antenna length and increases with the scan angle. This last result was not emphasized in previous investigations on 1-D bidirectional or 2-D LWAs [16], [21] for which the gain–bandwidth FoM is evaluated at broadside only, and thus is constant.

Another typical feature of PRS-based structures is that $\hat{\beta}$ and \hat{a} can no longer be varied freely, but are constrained to obey a particular relationship that depends on the PRS reflectivity. In this regard, we recall that leaky modes in PRS-based LWAs are often assumed to obey the hyperbolic relation $\hat{\beta}\hat{a} = C$, where C is a constant [13]. The first important result derived in this article is that this relation happens to be approximately true only for TM modes. For TE modes, the value of C considerably changes with frequency. Another important result of this article is the derivation of design formulas to properly set the cavity height and the PRS reactance in order to have a given $\hat{\beta}$ and \hat{a} at the design frequency for both the TM and TE cases. Therefore, the optimum \hat{a} for any given $\hat{\beta}$ and L provided in [7] translates into criteria to find the optimum PRS reactance and cavity height. Interestingly, it turns out that for each optimum set of $\hat{\beta}$ and \hat{a} values, we have a fourfold choice: an inductive/capacitive PRS for a TE/TM leaky mode.

All these findings are finally validated through numerical and full-wave simulations. We first consider a simplified, ideal model that matches well with the theory and then show that no relevant differences are obtained for a more realistic model that takes into account several practical aspects.

The manuscript is thus organized as follows. Section II briefly reviews the main results obtained in [7] that are exploited here. In Section III, formulas for evaluating the bandwidth performance and the gain–bandwidth FoM are derived, whereas in Section IV, it is shown that there exist four possible ways to optimize the gain of a PRS-based 1-D unidirectional LWA depending on whether an inductive/capacitive PRS and a TE/TM mode are used. In Section IV, design criteria to maximize the gain in each of these cases are reported, whereas a full-wave validation is presented in Section V for a specific, yet practical case: a rectangular waveguide based on a metal strip grating (MSG). Concluding remarks are finally drawn in Section VI.

II. FORMULAS FOR 1-D UNIDIRECTIONAL LWAS

We report here the main formulas of [7] that apply to any 1-D unidirectional LWA and that will prove to be useful to derive the optimum conditions for those based on PRSs. Namely: 1) the radiation pattern; 2) the half-power beamwidth; and 3) the gain. According to the discussion in [7, Sec. II], we limit our analysis to beams radiating not too close to endfire.

TABLE I
FITTING COEFFICIENTS FOR THE CORRECTION FUNCTION CF

c_{ij}	$j = 0$	$j = 1$	$j = 2$	$j = 3$
$i = 0$	0.888	-0.134	0.572	0.339
$i = 1$	0.280	0.001	-0.392	0.155
$i = 2$	1.172	-1.008	5.952	0.479

The normalized radiation pattern $P(\theta)$ is given by

$$P(\theta) = \frac{\sinh^2 a + \sin^2 t(\theta)}{a^2 + t(\theta)^2} \quad (1)$$

where θ is the elevation angle measured from the vertical z -axis and $t(\theta) = b - l \sin \theta$, with $l = k_0 L/2$, $b = \hat{\beta}l$, and $a = \hat{a}l$ are normalized variables. It is worthwhile to recall here that a is intimately related to the radiation efficiency through $e_r = 1 - \exp(-4a)$, and $\hat{\beta}$ to the beam angle θ_0 (defined as the angle of maximum radiated power, $P(\theta_0) = \max[P(\theta)]$) through the well-known relation $\hat{\beta} = \sin \theta_0$; this relation has been proved to remain exact even for truncated structures (as shown in Fig. 1) [22].

The double-sided beamwidth is given by

$$\Theta_h = \arcsin(\hat{\beta} + t_h(a)/l) - \arcsin(\hat{\beta} - t_h(a)/l) \quad (2)$$

where $t_h(a)$ is the value of t at the (left) half-power angle and is accurately expressed by the following formula [22]:

$$t_h(a) = t_0[1 - \tanh(u_1 a)] + a \tanh(u_2 a) \quad (3)$$

with $t_0 = 1.39156$, $u_1 = 0.021$, and $u_2 = 0.210$. (Henceforth, $t_h(a)$ is referred to as t_h .) We also recall that (2) holds for $\hat{\beta} < 1 - t_h/l$, that is, for beams not too close to endfire [7]. For scanned directive beams (2) is well approximated by

$$\Theta_h \simeq 2 \sec \theta_0 t_h(a)/l \sim 2\hat{a} \sec \theta_0 \quad (4)$$

where the last expression is obtained asymptotically for $L \rightarrow \infty$, keeping \hat{a} fixed. Finally, the gain is given by

$$G = \frac{4e_r \text{CF} \sec \theta_0}{\Theta_h} = \frac{2e_r \text{CF}}{t_h(a)/l} \quad (5)$$

where CF is a correction function that improves the otherwise inaccurate directivity–beamwidth relation, viz., $D \simeq 4 \sec \theta_0 / \Theta_h$ [7]. An accurate analytical expression for CF has been obtained through numerical fitting in [7] and is reported here for the sake of completeness as

$$\text{CF} = c_0 + c_1[\text{sech}(c_2 a) - 1] \quad (6)$$

where c_i for $i = 0, 1, 2$ are fitting functions of L/λ_0 and $\hat{\beta}$ given by the interpolation scheme $c_i = c_{i0} + (c_{i1} + c_{i2}\hat{\beta})e^{-c_{i3}L/\lambda_0}$, where c_{ij} for $j = 0, \dots, 3$ are fitting parameters and are reported in Table I. The combination of (3), (5), and (6) yields a compact formula for the gain as a function of a , $\hat{\beta}$, and L/λ_0 as

$$G \simeq \frac{k_0 L (1 - e^{-4a}) \{c_0 + c_1[\text{sech}(c_2 a) - 1]\}}{t_0 [1 - \tanh(0.021a)] + a \tanh(0.21a)} \quad (7)$$

where the dependence on $\hat{\beta}$ and L/λ_0 is implicit in the definition of c_i , $i = 0, 1, 2$. (Note that the factor $k_0 L$ was

mistakenly missing in [7, eq. (17)].) As $L \rightarrow \infty$, with $\hat{\alpha}$ fixed, (7) further simplifies, yielding the convenient formula [7]

$$G_\infty \simeq 1.2/\hat{\alpha}. \quad (8)$$

We recall that, if material losses have to be accounted for, one should replace (7) with [7, eq. (25)]. As extensively discussed in [7], material losses will only lead to a slightly different value of the optimum attenuation constant (or leakage rate), and in turn to a different choice of the optimum design parameters. However, the procedure described in Section IV-B will remain the same. For this reason, in this work, we only discuss the lossless case; the reader can find in [7] the modifications needed for the lossy case.

III. BANDWIDTH, GAIN, AND GAIN–BANDWIDTH FIGURE OF MERIT FOR PRS-BASED LWAs

As briefly commented in Section I, results from [7], which we also have summarized in Section II, have general validity and can be applied to any 1-D unidirectional LWAs. However, the bandwidth performance of a 1-D unidirectional LWA designed to maximize gain is structure-specific, as the definition of bandwidth requires knowledge of the leaky complex wavenumber dispersion over frequency f . In Section III-A, we derive approximate analytical expressions for both the fractional bandwidth (FBW) and the gain–bandwidth FoM for PRS-based LWAs, whereas in Section III-B, we comment on the overall performance that one can expect from the wide class of PRS-based 1-D unidirectional LWAs.

A. Analytical Formulas

The reference structure consists of a PRS-based 1-D unidirectional LWA of length L fed at one end and terminated with an ideal absorber (see Fig. 1).

In this regard, we recall that for LWAs based on a PRS, the optimum pair of $\hat{\beta}$ and $\hat{\alpha}$ values determines the optimum cavity height and PRS to have maximum gain at a given angle. In particular, for a highly reflective PRS, the cavity height mainly determines $\hat{\beta}$, whereas the PRS properties mainly determine $\hat{\alpha}$. In general, the PRS may affect both $\hat{\beta}$ and $\hat{\alpha}$, and the optimization procedure needs to account for this interdependence. The entire design flow for optimizing PRS-based 1-D unidirectional LWAs will be discussed in detail in Section IV.

Conversely, in Section III, we are interested in obtaining simple formulas for the FBW and the gain–bandwidth FoM. In this regard, the equivalent loss tangent introduced in [11]–[13] represents a simple, yet effective model to obtain an *analytical* dispersion equation of leaky modes propagating in PRS-based LWAs (which, otherwise, would require the numerical solution of a transcendental equation [23]). Indeed, an LWA can be thought as a lossy parallel-plate waveguide (PPW) where an equivalent loss tangent $\tan \delta_{\text{eq}}$ is conveniently defined to model all kinds of losses (including radiation losses) [11]–[13].

In particular, for a lossy PPW of height h and dielectric filling $\epsilon_r = \epsilon_r(1 - j \tan \delta)$, we have

$$\hat{k}_x = \sqrt{\epsilon_r(1 - j \tan \delta_{\text{eq}}) - (\pi/k_0 h)^2} \quad (9)$$

where a nonmagnetic material $\mu_r = 1$ is tacitly assumed.

In order to have the beam radiating at a given design scan angle $\theta_{\text{od}} \equiv \theta_0(f = f_0)$ at the design frequency f_0 , the cavity height can be set, at a first approximation (more accurate formulas are not needed here, but will be discussed in Section IV), equal to [8], [24]

$$h_{\text{ppw}} = \frac{\lambda_0}{2\sqrt{\epsilon_r - \sin^2 \theta_{\text{od}}}} \quad (10)$$

where the free-space wavelength λ_0 is here fixed at the design frequency f_0 . In addition, as can be inferred from Table II, in almost all cases, $\hat{\alpha}$ is more than an order of magnitude lower than $\hat{\beta} = \sin \theta_0$ (as long as we consider beams far from broadside); thus by squaring both sides of (9) [using $h = h_{\text{ppw}}$ as given by (10)] and taking the real part, we get

$$\hat{\beta} = \sin \theta_0 \simeq \sqrt{\epsilon_r - \frac{\epsilon_r - \sin^2 \theta_{\text{od}}}{\bar{f}^2}} \quad (11)$$

where $\bar{f} = f/f_0$ is a normalized frequency. From (11), an expression for \bar{f} as a function of θ_0 is easily found as

$$\bar{f}(\theta_0) \simeq \sqrt{\frac{\epsilon_r - \sin^2 \theta_{\text{od}}}{\epsilon_r - \sin^2 \theta_0}}. \quad (12)$$

Equation (12) will turn out to be useful to find an expression for the fractional bandwidth FBW as we will readily show.

Interestingly, an expression for the scan rate, expressed as the derivative of the beam angle with respect to the normalized frequency, can also be derived from (11) and reads

$$\frac{d\theta_0}{d\bar{f}} = \frac{\epsilon_r - \sin^2 \theta_{\text{od}}}{\sin \theta_{\text{od}} \cos \theta_{\text{od}}} \quad (13)$$

which for an air substrate simplifies to

$$\frac{d\theta_0}{d\bar{f}} = \cot \theta_{\text{od}}. \quad (14)$$

Both (13) and (14) clearly reveal that as the beam angle goes from broadside to endfire the scan rate decreases and in turn the -3 dB gain FBW is expected to increase. Interestingly, (13) and (14) also provide the angular range $\Delta\theta_0$ over which the beam scans within its FBW through the relation $\Delta\theta_0 = \text{FBW} \cot \theta_{\text{od}}$ in the air-filled case (a similar formula is obtained from (13) for the dielectric-filled case), according to the frequency-scanning behavior common to all LWAs. We recall that FBW is defined as $\text{FBW} = \bar{f}(\theta_{\text{od}} + \Delta\theta_{\text{h,l}}) - \bar{f}(\theta_{\text{od}} - \Delta\theta_{\text{h,r}})$, where $\Delta\theta_{\text{h,l}}(\Delta\theta_{\text{h,r}})$ represent the left(right)-sided -3 dB beamwidth. From the previous definition and (12), an analytic expression for FBW is obtained as

$$\begin{aligned} \text{FBW} &\simeq \sqrt{\epsilon_r - \sin^2 \theta_{\text{od}}} \\ &\times \left[\frac{1}{\sqrt{\epsilon_r - \sin^2(\theta_{\text{od}} + \Delta\theta_{\text{h,l}})}} - \frac{1}{\sqrt{\epsilon_r - \sin^2(\theta_{\text{od}} - \Delta\theta_{\text{h,r}})}} \right] \\ &\simeq \left[\frac{\sqrt{\epsilon_r - \hat{\beta}_{\text{od}}^2}}{\sqrt{\epsilon_r - (\hat{\beta}_{\text{od}} + t_{\text{h}}/l)^2}} - \frac{\sqrt{\epsilon_r - \hat{\beta}_{\text{od}}^2}}{\sqrt{\epsilon_r - (\hat{\beta}_{\text{od}} - t_{\text{h}}/l)^2}} \right] \quad (15) \end{aligned}$$

TABLE II

OPTIMUM NORMALIZED ATTENUATION CONSTANT $\hat{\alpha}_{\text{opt}}$, GAIN G , FBW, AND GAIN-BANDWIDTH FoM FOR AN OPTIMIZED AIR-FILLED PRS-BASED 1-D UNIDIRECTIONAL LWA FOR DIFFERENT DESIGN SCAN ANGLES θ_{0d} AND ANTENNA LENGTHS L/λ_0

L/λ_0	$\theta_{0d} = 15^\circ$				$\theta_{0d} = 30^\circ$				$\theta_{0d} = 45^\circ$				$\theta_{0d} = 60^\circ$			
	$\hat{\alpha}_{\text{opt}}$	G (dB)	FBW (%)	FoM	$\hat{\alpha}_{\text{opt}}$	G (dB)	FBW (%)	FoM	$\hat{\alpha}_{\text{opt}}$	G (dB)	FBW (%)	FoM	$\hat{\alpha}_{\text{opt}}$	G (dB)	FBW (%)	FoM
5	$4.11 \cdot 10^{-2}$	12.26	5.24	0.88	$4.14 \cdot 10^{-2}$	12.30	12.74	2.16	$4.21 \cdot 10^{-2}$	12.40	28.34	4.92	$4.49 \cdot 10^{-2}$	12.64	99.68	18.31
10	$2.03 \cdot 10^{-2}$	15.20	2.58	0.86	$2.03 \cdot 10^{-2}$	15.22	6.23	2.07	$2.05 \cdot 10^{-2}$	15.26	13.37	4.49	$2.10 \cdot 10^{-2}$	15.41	35.05	12.19
20	$1.01 \cdot 10^{-2}$	18.17	1.29	0.85	$1.01 \cdot 10^{-2}$	18.18	3.10	2.04	$1.01 \cdot 10^{-2}$	18.21	6.59	4.36	$1.03 \cdot 10^{-2}$	18.27	16.42	11.02
50	$4.01 \cdot 10^{-3}$	22.13	0.51	0.84	$4.01 \cdot 10^{-3}$	22.14	1.24	2.02	$4.02 \cdot 10^{-3}$	22.15	2.62	4.30	$4.04 \cdot 10^{-3}$	22.17	6.44	10.62
100	$2.00 \cdot 10^{-3}$	25.14	0.26	0.84	$2.00 \cdot 10^{-3}$	25.14	0.62	2.02	$2.01 \cdot 10^{-3}$	25.14	1.31	4.28	$2.01 \cdot 10^{-3}$	25.16	3.21	10.53
200	$1.00 \cdot 10^{-3}$	28.14	0.13	0.84	$1.00 \cdot 10^{-3}$	28.14	0.31	2.01	$1.00 \cdot 10^{-3}$	28.15	0.66	4.28	$1.00 \cdot 10^{-3}$	28.15	1.61	10.49
500	$0.40 \cdot 10^{-3}$	32.12	0.05	0.84	$0.40 \cdot 10^{-3}$	32.12	0.12	2.01	$0.40 \cdot 10^{-3}$	32.12	0.26	4.27	$0.40 \cdot 10^{-3}$	32.12	0.64	10.47

where $\hat{\beta}_{0d} = \sin \theta_{0d}$. In the last step, we used the fact that $t = \pm t_h$ is found at the lower and upper frequency edges, respectively, and also assumed that the beam has a negligible variation in shape as the beam scans with frequency over the bandwidth. (Note that the first term on the right-hand side of (15) might be singular. This singularity is related to the discontinuity angle discussed in [7] and thus care must be taken in using this formula for scan angles that approach endfire.) This expression (15) further simplifies for some particular cases of practical interest. Indeed, for directive, scanned, symmetric beams (i.e., $\Delta\theta_{h,r} = \Delta\theta_{h,l} \ll \theta_{0d}$), a first-order Taylor approximation allows for writing (15) as

$$\text{FBW} \simeq \frac{\Theta_h \sin \theta_{0d} \cos \theta_{0d}}{\varepsilon_r - \sin^2 \theta_{0d}} \simeq \frac{2\hat{\beta}_{0d}(t_h/l)}{\varepsilon_r - \hat{\beta}_{0d}^2} \quad (16)$$

which, for the infinite case, $L \rightarrow \infty$, simplifies to

$$\text{FBW}_{\text{inf}} \simeq \frac{2\hat{\beta}_{0d}\hat{\alpha}}{\varepsilon_r - \hat{\beta}_{0d}^2}. \quad (17)$$

Moreover, for air-filled LWAs (i.e., $\varepsilon_r = 1$), a very simple expression is found from (16), which reads

$$\text{FBW}_{\text{air}} \simeq \Theta_h \tan \theta_{0d}. \quad (18)$$

As a result, the gain-bandwidth FoM, which is defined as $\text{FoM} = G \cdot \text{FBW}$, is accurately obtained by multiplying (15) and (5). For directive 1-D unidirectional LWAs based on PRSs, an even simpler expression for FoM is found by combining (16) and (5) to obtain

$$\text{FoM} = 4e_r \text{CF} \frac{\sin \theta_{0d}}{\varepsilon_r - \sin^2 \theta_{0d}} \quad (19)$$

which, in the air-filled case reduces to

$$\text{FoM}_{\text{air}} = 4e_r \text{CF} \tan \theta_{0d} \sec \theta_{0d}. \quad (20)$$

We recall that the previous expressions (16)–(20) do not hold for $\theta_{0d} \rightarrow 0^\circ$. However, broadside radiation is rather impractical for most of 1-D unidirectional LWAs (Dirac LWAs [6] represent a peculiar case), and thus this aspect is of little consequence here.

A remark is also needed about the definition of bandwidth employed here. Indeed, FBW is meant here as a fractional pattern bandwidth. Nonetheless, the bandwidth performance of an antenna is established as the minimum between the impedance bandwidth and the pattern bandwidth. Usually, the latter is narrower than the former for an LWA, and thus the bandwidth of an LWA is mostly determined by its pattern bandwidth. However, as revealed by the analysis reported in Section III-B (see Table II), there exist operating conditions for which the pattern bandwidth can even attain an octave. Over such a large bandwidth, it could be difficult to achieve a good impedance matching, and a more detailed analysis of the feeding techniques of 1-D unidirectional LWAs would be required. This aspect, although important, requires a case-by-case analysis that goes beyond the scope of this work and is thus not treated here. As a result, the bandwidth performance reported in the following results is related only to the pattern bandwidth.

B. Optimization of LWA Performance

In Table II, we have reported the values of G , FBW, and FoM for different antenna lengths and design scan angles under the conditions of optimum gain derived in [7]. The values of G are obtained numerically, whereas those of FBW and FoM result from a straight implementation of (15) and (19), respectively; we will soon comment on the expected accuracy of these formulas.

The values of G reported in Table II are a consequence of the optimization carried out in [7]. This result further confirms that the gain of a 1-D unidirectional LWA increases almost linearly with the antenna length and is almost independent of the design scan angle [as expected from (5)].

As concerns FBW and FoM, Table II shows that the FBW decreases in the optimum design (optimized for maximum gain) as the aperture length (and hence the maximum gain) increases. The FoM approaches a limit as the aperture length increases in the optimum design. This limit only depends on the design scan angle and increases as the design scan angle increases.

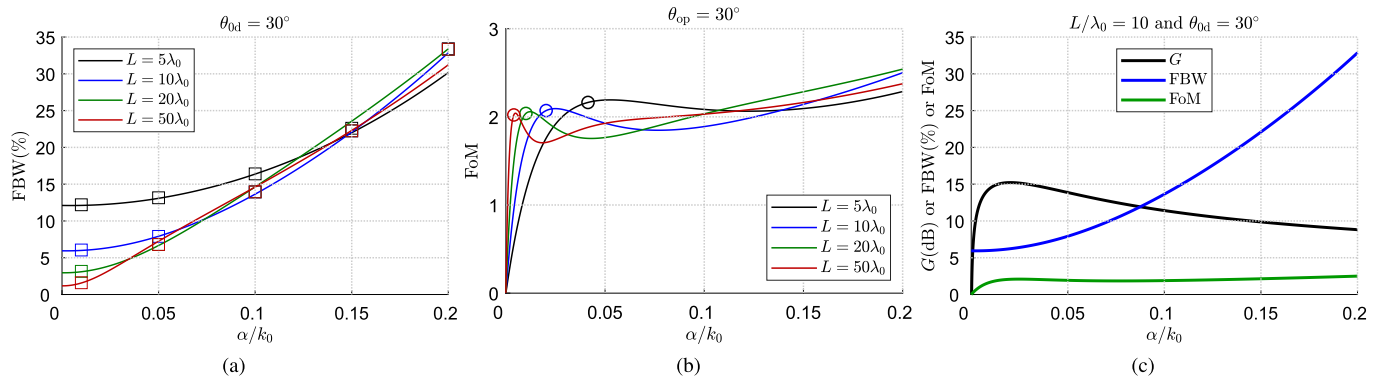


Fig. 2. (a) FBW and (b) gain–bandwidth FoM as functions of the normalized attenuation constant $\hat{\alpha}$ for $\theta_{od} = 30^\circ$ for different values of $L/\lambda_0 = 5, 10, 20, 50$ (in black, blue, green, and red, respectively). In (a), FBW as calculated through (15) is compared with numerical results (in squares) from the evaluation of the exact -3 dB points of the gain pattern. In (b), the FoM is calculated through the product of equations (5) and (15) and reported in solid lines. In (c), colored circles identify the condition for maximum gain, which is apparently close to a local maximum for the FoM. In (c), numerical evaluations of G , FBW, and FoM versus α/k_0 are reported on the same plot for $\theta_{od} = 30^\circ$ and $L = 10\lambda_0$.

If we regard the normalized attenuation constant $\hat{\alpha}$ to be a free variable and not constrained to optimize the gain, then Fig. 2(a)–(c) shows the variation of FBW, FoM, and G versus $\hat{\alpha}$ for various aperture lengths. We also note that both FBW and FoM increase with $\hat{\alpha}$ [see Fig. 2(a) and (b)], and this result can also be inferred from the formulas reported in Section III-A, for FBW and FoM. Indeed, as concerns the FBW, for electrically large apertures, we have $t_h/l \rightarrow \hat{\alpha}$, thus FBW in (16) is asymptotically proportional to $\hat{\alpha}$. On the other hand, the FoM, for a fixed beam angle, only depends on CF and e_r ; the former mildly depends on $\hat{\alpha}$, while the latter increases with $\hat{\alpha}$.

We should now comment on the accuracy of (15), which is confirmed by the numerical evaluations of FBW from the -3 dB gain pattern for $L/\lambda_0 = 5, 10, 20, 50$ and $\hat{\alpha} = 0.01, 0.05, 0.1, 0.15, 0.2$ [see the colored squares in 2(a)]. Numerical results are obtained by determining the -3 dB points from the evaluation of the gain [calculated through the numerical integration of (1)] over a suitable frequency range, over which we assume the leakage rate to be constant and the normalized phase constant to change according to the dispersion relation in (11). These assumptions will be demonstrated to agree well with full-wave simulations in Section V.

As expected, the absolute error is negligible for lower values of $\hat{\alpha}$ and larger values of L/λ_0 , whereas it slightly increases for opposite conditions, where, however, absolute differences between the numerical values and those provided by (15) remain lower than approximately 1%, and the percent error is always lower than 10%. (Note that the percent error of the FoM is the same as the FBW, since the gain is evaluated numerically.)

Similar results are found for different beam angles and more numerical and full-wave validations (not shown for brevity) have been performed for different operating conditions, confirming the consistency among all results. We can also confirm that the approximate expression in (18) agrees very well with that in (15) under the hypothesis of small beamwidth, that is, for small $\hat{\alpha}$, namely $\hat{\alpha} < 0.05$. The error in (18) is larger for larger values of $\hat{\alpha}$, but it is still small for those values of $\hat{\alpha}$ that would be used to maximize the gain, viz., $\hat{\alpha}_{opt}$. In this regard, we should comment that the

numerical evaluation of the FBW performed here assumes that the frequency dispersion of the normalized phase constant (or, equivalently, the scan angle) is given by (11). In practice, the dispersion curve of a leaky mode propagating in a PRS-based 1-D unidirectional LWA may differ from that approximate equation, viz. (11), especially when the leakage rate is not small (namely for $\hat{\alpha} > 0.05$). This aspect requires specific attention and thus will be treated in detail in Sections IV-A and V-A.

Incidentally, we note that the condition for maximum gain is very close to a local maximum for the FoM. This is clearly manifest in Fig. 2(c), where G , FBW, and FoM versus $\hat{\alpha}$ are reported on a single plot for the representative case of $\theta_{od} = 30^\circ$ and $L/\lambda_0 = 10$. The gain and the FBW have opposite trends except for low values of $\hat{\alpha}$, where they both increase. This behavior determines the almost constant character of the FoM for intermediate values of $\hat{\alpha}$. For low values of $\hat{\alpha}$, the FBW is rather flat and the FoM behavior is substantially determined by G , thus showing a mild local maximum. For high values of $\hat{\alpha}$, G decreases (this is consistent with the quasi-linear dependence of the beamwidth on $\hat{\alpha}$), but the higher growth rate of FBW determines the slightly increasing character of the FoM.

As a result, while there exists $\hat{\alpha}_{opt}$ that maximizes the gain (see Table II), there is no optimum attenuation constant to maximize the FBW: the larger the attenuation constant, the larger the FBW. However, LWAs do not work properly for large values of $\hat{\alpha}$ (in practice, for $\hat{\alpha} > 0.2k_0$, the leaky-wave contribution to the total aperture field might no longer be dominant, see [25]) where they also exhibit poor gain. In addition, as we discussed at the end of Section III-A, the actual bandwidth is also limited by the impedance bandwidth, thus making ineffective the pattern bandwidth enhancement for large values of $\hat{\alpha}$.

Another calculation of interest is to determine the maximum FBW that can be achieved given a minimum gain constraint and vice versa, that is, what is the maximum gain that can be achieved given a minimum FBW. For this purpose, we show in Fig. 3(a) the maximum FBW as a function of a minimum gain constraint, and in Fig. 3(b) the maximum gain as a function of a minimum FBW constraint for an air-filled 1-D

unidirectional of length $L = 10\lambda_0$ and different design scan angles. These plots were obtained by sweeping $\hat{\alpha}$ and finding the optimum value that maximized the quantity of interest while satisfying the constraint. The results are compared for the infinite case (colored dashed lines) and show that both the maximum FBW and the maximum gain are monotonically decreasing functions of the minimum gain and minimum FBW constraints, respectively.

In Fig. 3(a), the curves for $L = 10\lambda_0$ are correctly interrupted when the minimum gain is about 15 dB: this is indeed the maximum gain that one can get out of a 1-D unidirectional LWA of length $L = 10\lambda_0$ for any scan angle (see Table II). Accordingly, in Fig. 3(b), the curves for $L = 10\lambda_0$ remain constant and equal to about 15 dB, as long as the minimum FBW constraint is lower than the maximum FBW obtained for the corresponding minimum gain constraint of 15 dB [cf. Fig. 3(a)].

On the other hand, for an infinite 1-D unidirectional LWA [dashed lines in Fig. 3(a) and (b)], the maximum FBW slowly decreases to zero as the minimum gain constraint increases. In both the infinite and finite cases, however, for a low minimum gain constraint, the maximum FBW asymptotically increases, but this usually requires unpractical values of $\hat{\alpha}$ as commented above. Correspondingly, for a large minimum FBW constraint, the maximum gain slowly decreases and eventually drops to 0 (not shown), but again this usually requires unpractical values of $\hat{\alpha}$ for which a leaky-wave analysis is no longer appropriate. We finally note that the simple relations between G (8) and FBW (16) for an infinite, air-filled 1-D unidirectional LWA allow for a simple analytic formula to recover the dashed colored curves reported in Fig. 3(a) and (b), and that reads

$$\text{FBW}_{\text{air},\infty} \simeq \frac{2.4}{G} \tan \theta_{\text{od}} \sec \theta_{\text{od}}. \quad (21)$$

IV. DESIGN FORMULAS FOR THE CAVITY HEIGHT AND THE PRS REACTANCE

Section IV aims at providing analytic expressions for correctly setting the cavity height and the PRS sheet reactance to support the required leaky wavenumber to have maximum gain at a given frequency, and to evaluate the scan performance over a certain frequency range.

To this aim, and without loss of generality, we first consider a dielectric-filled PPW of height h where the upper metallic plate is replaced by a lossless, thin PRS characterized by a single, scalar, purely imaginary sheet impedance $Z_s = jX_s$ (see Fig. 4, left). (Note that the transverse equivalent network model in Fig. 4, right, assumes an infinite “baffle”; more comments on this are given in Section V.) Typical subresonant gratings of fishnet/cermet-like unit-cells fulfill this hypothesis (viz., $Z_s = jX_s$) and for certain elementary topologies analytical expressions are available (e.g., [26], [27]). Nonetheless, the results of Section IV can easily be extended to account for the more general case of a thick PRS (as shown in Appendix A).

The results apply directly to common 1-D LWAs that implicitly make use of the PRS concept, such as the holey and the slitted waveguides [7], [28]. For these structures, expressions are available for the complex surface impedance that

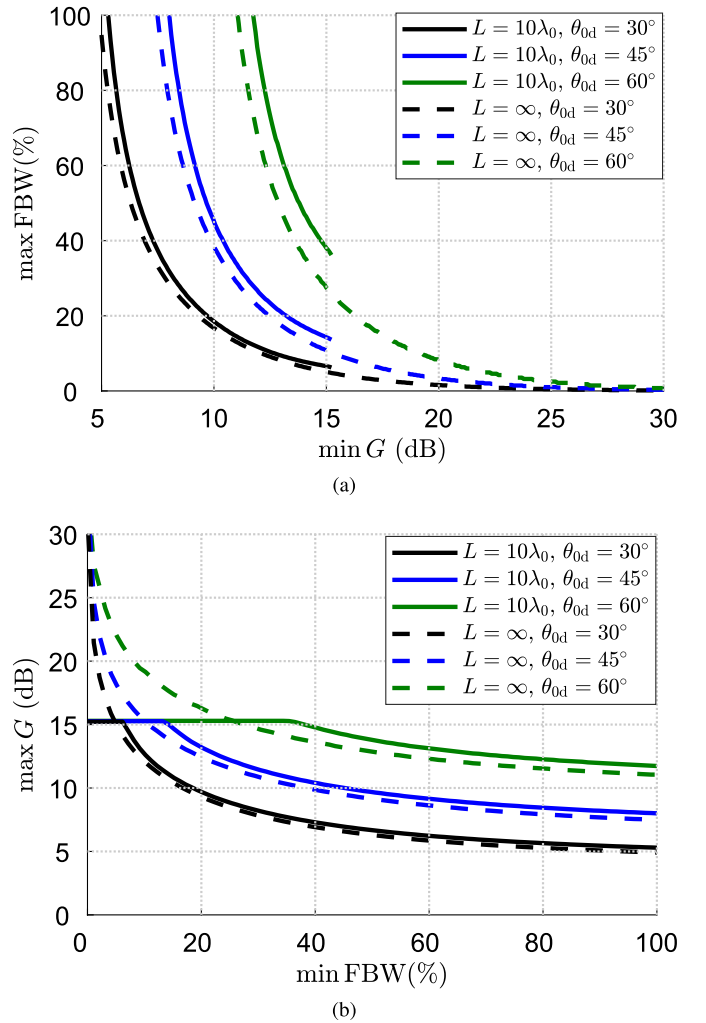


Fig. 3. (a) Maximum FBW versus minimum gain constraint, and (b) maximum gain versus minimum FBW constraint for an air-filled 1-D unidirectional LWA of length $L = 10\lambda_0$ (solid colored lines) and infinite length (dashed colored lines) and different design scan angles.

accounts for both the internal and external impedances characterizing the discontinuity. Therefore, one has to de-embed the contribution due to radiation in free space to recover a purely imaginary PRS sheet impedance: the optimum design rules provided in Section IV-B apply to this quantity.

We first comment on the different dispersive behaviors of TE and TM leaky modes in PRS-based unidirectional LWAs and their effect on the bandwidth performance (see Section IV-A). As a result, design equations for both the PRS and the cavity height (see Section IV-B) are different for TE and TM leaky modes. The inductive/capacitive character of the PRS is also accounted for, and thus it is seen that for each optimum condition, we have a four-fold choice: inductive/capacitive PRS and TE/TM leaky mode (see Section IV-A). The results of Sections IV-A and IV-B find immediate application in Section IV-C where they are used to determine the scan performance of PRS-based unidirectional LWAs.

A. PRS Properties

In Section I, we commented that for a PRS-based LWA $\hat{\beta}$ and $\hat{\alpha}$ are constrained to obey a particular relation. In the

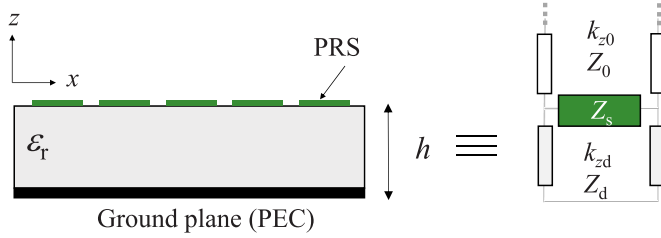


Fig. 4. Cross-sectional view of a dielectric-filled PPW of thickness h , where the upper plate is replaced by a PRS with sheet impedance Z_s (left) and its transverse equivalent network (right).

literature (see [11], [13], [16] and related works), it is assumed that the fundamental TE/TM leaky mode pair propagating in a PRS-based LWA obeys a hyperbolic relation of the type $\hat{\beta}\hat{a} = C$, where C is a constant that depends on the PRS reflectivity. We now show that this assumption turns out to be accurate only close to broadside where the TE/TM leaky wavenumbers are very similar to each other; as the scan angle increases, C remains remarkably constant in the TM case, but not anymore in the TE case. This aspect plays a key role in the correct design of PRS-based LWAs as we will discuss in more detail in Section IV-B.

Since the dispersive properties of the leaky modes are not affected by the antenna truncation, a simple way to obtain an approximate expression of the PRS constant as a function of the scan angle in the TM and the TE cases comes from retrieving an expression for \hat{a} from (4) in the infinite case and by exploiting the expressions for the beamwidths of an infinite-length PRS-based LWA [29, eqs. (23) and (25)]. With these expressions at hand, one finds that the PRS constant C takes the following two different expressions in the TE or TM case:

$$C^{\text{TE}} = C_b \cos \theta_0 \sqrt{(1 - \sin^2 \theta_0 / \epsilon_r)^3} \stackrel{\epsilon_r=1}{=} C_b \cos^4 \theta_0 \quad (22a)$$

$$C^{\text{TM}} = C_b \sec \theta_0 \sqrt{1 - \sin^2 \theta_0 / \epsilon_r} \stackrel{\epsilon_r=1}{=} C_b \quad (22b)$$

where $C_b = C^{\text{TE}}|_{\theta_0=0} = C^{\text{TM}}|_{\theta_0=0}$ is the value of the PRS constant at broadside and reads

$$C_b \equiv \frac{X_s^2 \sqrt{\epsilon_r^3}}{\pi \eta_0^2} \quad (23)$$

with $\eta_0 \simeq 120\pi \Omega$ being the free-space impedance. It is clear from (22a) and (22b) that C^{TE} strongly depends on the scan angle, whereas C^{TM} is almost independent for small permittivities. This is even more evident in the air-filled case, where $C^{\text{TE}} \propto \cos^4 \theta_0$ and C^{TM} is indeed constant. Moreover, (22a)–(22b) also reveal that close to broadside C^{TE} and C^{TM} are both approximately constant and equal to C_b . It is worthwhile noting here that C_b only depends on X_s and ϵ_r , that is, the physical properties of the structure. Thus, C_b is associated with the PRS only.

We also note that the expression for C_b in (23) coincides with that in [11, eq. (18)] in the lossless case (i.e., $Z_s = jX_s$ and $\tan \delta = 0$) and in the limit of a highly reflective thin PRS, that is, $|X_s| \ll \eta_0$. The original expression, viz., [11, eq. (18)], holds even for the lossy case and moderately reflective thin PRS; this more general expression will turn

to be useful to deal with thick PRSs [19], [20] as discussed in Appendix A.

We should comment that in LWAs, the scan angle typically changes with frequency, thus the dependence of the PRS constant on the scan angle implies a dependence on frequency, which may affect somehow the bandwidth properties of the antenna. However, the PRS itself, by virtue of Foster's reactance theorem [30]–[32] will also exhibit a sheet impedance that depends on frequency. The sheet impedance may also exhibit spatial dispersion, that is, the dependence from the scan angle [4], [27], [33]. Including a frequency-dispersive and spatially dispersive model for the sheet impedance, even for the simplest type of inductive/capacitive-like behaviors, does not allow for straightforward analytical treatment. Nevertheless, we will show in Section V with full-wave results that the formulas derived so far work remarkably well in practical cases, since the bandwidth is fairly small when the beam is narrow.

B. Design Formulas

Table II provides the optimum values of \hat{a} to get maximum gain at different scan angles (thus for different values of $\hat{\beta}$) from a PRS-based 1-D unidirectional LWA, as derived in [7]. However, we have not yet discussed how to obtain a given pair of $\hat{\beta}$ and \hat{a} at a given frequency from this class of LWAs. This task requires an accurate leaky-wave dispersion analysis.

With reference to the structure depicted in Fig. 4 along with its transverse equivalent network, the dispersion equations for the TE and TM modes are given, as is customary, through the application of the transverse resonance technique [34] to the TEN, and read

$$\text{(TE)} : j\hat{k}_{z0} + \eta_0/X_s + \hat{k}_{zd} \cot(k_0 \hat{k}_{zd} h) = 0 \quad (24a)$$

$$\text{(TE)} : j\hat{k}_{z0}^{-1} + \eta_0/X_s + \epsilon_r \hat{k}_{zd}^{-1} \cot(k_0 \hat{k}_{zd} h) = 0 \quad (24b)$$

where $\hat{k}_{z0} = (1 - \hat{k}_x^2)^{1/2}$ and $\hat{k}_{zd} = (\epsilon_r - \hat{k}_x^2)^{1/2}$ are the normalized vertical wavenumbers in the air and in the dielectric, respectively. A remark is needed here about the choice of the principal square root in the definition of the vertical wavenumbers. As is well known, the square root for \hat{k}_{z0} introduces a pair of branch points at $\hat{k}_x = \pm 1$ (the dispersion equations (24a), (24b) are even functions of \hat{k}_{zd} , and thus the corresponding choice of the square root is immaterial). The functions on the left-hand side of (24a) and (24b) are analytic and single-valued over a two-sheeted Riemann surface whose proper ($\text{Im}[\hat{k}_{z0}] < 0$) and improper ($\text{Im}[\hat{k}_{z0}] > 0$) sheets are typically connected through the Sommerfeld branch cuts [25], [35]. It can be shown that, when k_x is in the fourth quadrant (as we assume here), the principal square root choice that we tacitly made for k_{z0} always gives the improper choice, and thus a leaky mode [25], [35].

In most works dealing with LWAs, the dispersion equations (24a) and (24b) are typically solved for a fixed X_s and h . Therefore, the wavenumber dispersion, that is, $\hat{\beta}$ and \hat{a} versus f , of the fundamental TE–TM leaky mode pair has to be found numerically, searching for the complex roots of (24a) and (24b). Here, we are interested in solving the other way around: for a fixed pair of $\hat{\beta}$ and \hat{a} at the design frequency f_0 ,

TABLE III

OPTIMUM $\hat{\alpha}$, X_s , AND h/h_{ppw} FOR BOTH THE TE AND THE TM MODES (UPPER BOX: INDUCTIVE CHOICE, LOWER BOX: CAPACITIVE CHOICE), FOR AN OPTIMIZED AIR-FILLED PRS-BASED 1-D UNIDIRECTIONAL LWA FOR DIFFERENT DESIGN SCAN ANGLES θ_{0d} AND ANTENNA LENGTHS L/λ_0

$\frac{L}{\lambda_0}$	$\hat{\alpha}_{opt}$	$\theta_{0d} = 15^\circ$				$\hat{\alpha}_{opt}$	$\theta_{0d} = 30^\circ$				$\hat{\alpha}_{opt}$	$\theta_{0d} = 45^\circ$				$\hat{\alpha}_{opt}$	$\theta_{0d} = 60^\circ$			
		X_s^{TE} (Ω)	X_s^{TM} (Ω)	$\frac{h^{TE}}{h_{ppw}}$	$\frac{h^{TM}}{h_{ppw}}$		X_s^{TE} (Ω)	X_s^{TM} (Ω)	$\frac{h^{TE}}{h_{ppw}}$	$\frac{h^{TM}}{h_{ppw}}$		X_s^{TE} (Ω)	X_s^{TM} (Ω)	$\frac{h^{TE}}{h_{ppw}}$	$\frac{h^{TM}}{h_{ppw}}$		X_s^{TE} (Ω)	X_s^{TM} (Ω)	$\frac{h^{TE}}{h_{ppw}}$	$\frac{h^{TM}}{h_{ppw}}$
5	$4.11 \cdot 10^{-2}$	76.2	67.3	0.940	0.943	$4.14 \cdot 10^{-2}$	138	95.5	0.907	0.916	$4.21 \cdot 10^{-2}$	268	122	0.866	0.884	$4.49 \cdot 10^{-2}$	751	179	0.790	0.834
		-76.5	-75.9	1.058	1.062		-141	-116	1.089	1.098		-288	-163	1.1236	1.142		-1000	-308	1.156	1.205
10	$2.03 \cdot 10^{-2}$	52.6	47.2	0.958	0.959	$2.03 \cdot 10^{-2}$	93.2	65.7	0.935	0.939	$2.05 \cdot 10^{-2}$	174	80.1	0.906	0.914	$2.10 \cdot 10^{-2}$	434	98.1	0.854	0.875
		-52.7	-51.5	1.042	1.044		-93.9	-75.1	1.064	1.069		-178	-97.6	1.092	1.101		-477	-137	1.133	1.157
20	$1.01 \cdot 10^{-2}$	36.9	33.2	0.970	0.971	$1.01 \cdot 10^{-2}$	64.5	46.1	0.954	0.956	$1.01 \cdot 10^{-2}$	118	55.1	0.933	0.938	$1.03 \cdot 10^{-2}$	278	63.4	0.896	0.907
		-37.0	-35.4	1.030	1.030		-64.7	-50.7	1.046	1.048		-118	-63.2	1.066	1.071		-287	-79.3	1.101	1.113
50	$4.01 \cdot 10^{-3}$	23.2	21.2	0.981	0.982	$4.01 \cdot 10^{-3}$	40.2	29.4	0.971	0.972	$4.02 \cdot 10^{-3}$	72.5	34.7	0.958	0.959	$4.04 \cdot 10^{-3}$	164	38.6	0.934	0.938
		-23.1	-22.0	1.019	1.019		-40.2	-31.0	1.029	1.030		-72.6	-37.8	1.042	1.044		-166	-44.2	1.066	1.070
100	$2.00 \cdot 10^{-3}$	16.3	15.0	0.987	0.987	$2.00 \cdot 10^{-3}$	28.3	20.8	0.980	0.980	$2.01 \cdot 10^{-3}$	50.8	24.7	0.970	0.971	$2.01 \cdot 10^{-3}$	114	27.2	0.953	0.955
		-16.2	-15.4	1.013	1.013		-28.2	-21.7	1.020	1.021		-50.9	-26.1	1.030	1.031		-114	-29.9	1.047	1.049
200	$1.00 \cdot 10^{-3}$	11.6	10.6	0.991	0.991	$1.00 \cdot 10^{-3}$	19.9	14.8	0.985	0.986	$1.00 \cdot 10^{-3}$	35.8	17.5	0.979	0.979	$1.00 \cdot 10^{-3}$	79.5	19.2	0.967	0.968
		-11.6	-10.8	1.009	1.009		-20.01	-15.21	1.015	1.015		-35.8	-18.2	1.021	1.022		-79.6	-20.6	1.033	1.034
500	$0.40 \cdot 10^{-3}$	7.35	6.73	0.994	0.994	$0.40 \cdot 10^{-3}$	12.6	9.48	0.991	0.991	$0.40 \cdot 10^{-3}$	22.5	11.1	0.987	0.987	$0.40 \cdot 10^{-3}$	50.0	12.2	0.979	0.979
		-7.35	-6.86	1.006	1.006		-12.6	-9.48	1.009	1.009		-22.5	-11.5	1.013	1.014		-50.0	-12.7	1.021	1.021

we want to find the optimum X_s and h . As commented above, this would, in general, require us to numerically solve (24a) and (24b) over the 2-D space parameter of X_s and h , as exact analytical expressions of the form $X_s(\hat{\beta}, \hat{\alpha})$ and $h(\hat{\beta}, \hat{\alpha})$ cannot be derived straightforward from (24a) to (24b).

One of the main results of this work is represented by Table III, which reports, for different practical combinations of antenna length and desired scan angle, the optimum values of reactance sheet and cavity height to get the maximum gain. The numerical values reported in Table III are obtained through the above-mentioned 2-D numerical search ("Num. 2-D" in Table IV) in the air-filled case, but the formulas have been tested and proven accurate also in dielectric-filled cases (not reported).

However, a blind 2-D numerical search over large ranges for the two parameters might be either computationally expensive (for a fine discretization of the intervals) or lead to inaccurate results (for a rough discretization of the intervals). One possibility is to reduce the dimensionality of the problem to a 1-D numerical search. This approach can be performed by taking the imaginary part of (24a) and (24b): the zeros of the resulting equations define an implicit function of h only, thus reducing the problem to a 1-D numerical search ("Num. 1-D" in Table IV). The solutions for X_s are then found by taking the real part of (24a) and (24b), yielding

$$X_s^{TE} = \text{Re} \left[\frac{-\eta_0}{j\hat{k}_{z0,op} + \hat{k}_{zd,op} \cot(2\pi\hat{k}_{zd,op}h/\lambda_0)} \right] \quad (25a)$$

$$X_s^{TM} = \text{Re} \left[\frac{-\eta_0\hat{k}_{z0,op}\hat{k}_{zd,op}}{j\hat{k}_{zd,op} + \hat{k}_{z0,op}\epsilon_r \cot(2\pi\hat{k}_{zd,op}h/\lambda_0)} \right] \quad (25b)$$

where $\hat{k}_{z0,op} \equiv \hat{k}_{z0}(f_0)$, $\hat{k}_{zd,op} \equiv \hat{k}_{zd}(f_0)$, and λ_0 is at the design frequency, and then plugging in the numerical values for h found from the above-mentioned numerical 1-D search.

This approach can lead to very accurate results (we discuss the accuracy of all the proposed methods later in Section IV-B), but still requires a 1-D numerical search. The same accuracy can also be reached with a simple procedure based on an iterative method ("Ite." in Table IV), provided that a good initial guess is chosen. To this aim, we first obtain approximate analytic expressions for the optimum sheet reactances X_s^{TE} , X_s^{TM} . For a given pair of $\hat{\beta}$ and $\hat{\alpha}$, C^{TE} and C^{TM} are uniquely determined, hence from (22a) and (22b) we get

$$|X_s^{TE}| = \eta_0 \frac{\sqrt{\frac{\pi\hat{\beta}\hat{\alpha}\sec\theta_0}{\sqrt{(\epsilon_r - \sin^2\theta_0)^3}}}}{\epsilon_r=1} \eta_0 \frac{\sqrt{\pi\hat{\beta}\hat{\alpha}}}{\cos^2\theta_0} \quad (26a)$$

$$|X_s^{TM}| = \eta_0 \frac{\sqrt{\frac{\pi\hat{\beta}\hat{\alpha}\cos\theta_0}{\epsilon_r\sqrt{\epsilon_r - \sin^2\theta_0}}}}{\epsilon_r=1} \eta_0 \sqrt{\pi\hat{\beta}\hat{\alpha}}. \quad (26b)$$

However, the derivation of (26a) and (26b) does not distinguish between the capacitive/inductive nature of the PRS, which explains the modulus sign on the left-hand side of (26a) and (26b). When the PRS is highly reflective, the optimum reactance sheet values for the inductive/capacitive case are actually symmetric with respect to the origin, and this approximation is thus fairly accurate. One can easily check from the numerical results of Table III that (26a) and (26b) yield very accurate results close to broadside, and even at larger design scan angles provided the antenna length is sufficiently large to still require a highly reflective PRS to optimize the gain.

TABLE IV

COMPARISON BETWEEN DIFFERENT METHODS FOR OBTAINING THE OPTIMUM DESIGN PARAMETERS FOR $L = 10\lambda_0$ AND $\theta_{0d} = 30^\circ$

Method	$X_s \gtrless 0$	$L = 10\lambda_0, \theta_{0d} = 30^\circ$				$L = 20\lambda_0, \theta_{0d} = 60^\circ$			
		$X_s^{\text{TE}} (\Omega)$	$X_s^{\text{TM}} (\Omega)$	$h_{\text{ppw}}^{\text{TE}}$	$h_{\text{ppw}}^{\text{TM}}$	$X_s^{\text{TE}} (\Omega)$	$X_s^{\text{TM}} (\Omega)$	$h_{\text{ppw}}^{\text{TE}}$	$h_{\text{ppw}}^{\text{TM}}$
Num. 2-D	> 0	93.24	65.66	0.935	0.939	277.99	63.44	0.896	0.907
	< 0	-93.91	-75.08	1.064	1.069	-287.33	-79.21	1.101	1.113
Num. 1-D	> 0	93.22	65.73	0.935	0.939	278.09	63.49	0.896	0.907
	< 0	-93.92	-75.08	1.064	1.069	-287.24	-79.25	1.101	1.113
Ite.	> 0	93.22	65.73	0.935	0.939	278.09	63.49	0.896	0.907
	< 0	-93.92	-75.08	1.064	1.069	-287.24	-79.25	1.101	1.113
Ana.	> 0	91.33	64.5	0.935	0.939	263.71	60.58	0.898	0.909
	< 0	-91.85	-73.31	1.064	1.068	-270.46	-74.01	1.098	1.110

Now that we have expressions for the optimum reactance sheet X_s , formulas for the optimum cavity heights in both the TE and TM cases can directly be derived from (24a) to (24b), leading to

$$h_{\text{TE}} = \text{Re} \left\{ \frac{\lambda_0}{2\hat{k}_{z0,\text{op}}} \left[1 - \frac{1}{\pi} \cot^{-1} \left(\frac{\eta_0 + jX_s \hat{k}_{z0,\text{op}}}{X_s \hat{k}_{z0,\text{op}}} \right) \right] \right\} \quad (27a)$$

$$h_{\text{TM}} = \text{Re} \left\{ \frac{\lambda_0}{2\hat{k}_{z0,\text{op}}} \left[1 - \frac{1}{\pi} \cot^{-1} \left(\frac{\eta_0 + jX_s / \hat{k}_{z0,\text{op}}}{\epsilon_r X_s / \hat{k}_{z0,\text{op}}} \right) \right] \right\}. \quad (27b)$$

Note that the range of the inverse cotangent function is assumed here to lie between $-\pi/2$ and $\pi/2$. The values of $\pm X_s^{\text{TE}}$ and $\pm X_s^{\text{TM}}$ provided by (26a) and (26b) can then be used as initial guesses in (27a) and (27b) to get a first estimate of h_{TE} and h_{TM} ; these values can then be used in (25a) and (25b) to get a better estimation of $\pm X_s^{\text{TE}}$ and $\pm X_s^{\text{TM}}$ and so on. Such an iterative process, based on (27a) and (27b) and (25a) and (25b), reaches a satisfactory accuracy after few steps. From Table IV, it is manifest that the iterative process fully converges to the results of the numerical 1-D method. (The results of ‘‘Ite.’’ in Table IV have been obtained with less than 40 iterations, with a convergence stop criterion set to $\Delta\epsilon = 0.001\%$, where $\Delta\epsilon$ is the relative percent difference between consecutive iterations.) Nevertheless, the X_s values obtained with the numerical 2-D search are slightly different from those obtained with the numerical 1-D and the iterative method, whereas the h values coincide. This behavior is mainly due to the different sensitivity of the dispersion equation with respect to variations of either X_s or h from the points of global minimum: a small change of h would require a significant change in X_s to meet the resonance condition. Conversely, significant changes in X_s would require only moderate changes in h . This sensitivity is also reflected by (27a) and (27b), and (25a) and (25b), which reveal that h varies with $\cot^{-1}(\cdot)$ and X_s varies with $\cot(\cdot)$, respectively.

The general expressions in (27a) and (27b) can greatly be simplified when specialized for scanned beams in the limit of a highly reflective PRS, that is, $X_s \ll \eta_0$. In this case, $\hat{\beta} \gg \alpha$ and (27a) and (27b) simplify as

$$h_{\text{TE}}^{\text{scan}} \simeq \frac{\lambda_0}{2\sqrt{\epsilon_r - \sin^2 \theta_{0d}}} \left[1 - \frac{1}{\pi} \cot^{-1} \left(\frac{(\eta_0 / X_s)}{\sqrt{\epsilon_r - \sin^2 \theta_{0d}}} \right) \right] \quad (28a)$$

$$h_{\text{TM}}^{\text{scan}} \simeq \frac{\lambda_0}{2\sqrt{\epsilon_r - \sin^2 \theta_{0d}}} \left[1 - \frac{1}{\pi} \cot^{-1} \left(\frac{\sqrt{\epsilon_r - \sin^2 \theta_{0d}}}{\epsilon_r (X_s / \eta_0)} \right) \right] \quad (28b)$$

where the contribution of dielectric losses has safely been ignored. It is worth noting that the inverse cotangent is an odd function and hence the inductive/capacitive ($X_s \gtrless 0$) nature of the sheet impedance shifts downward/upward the design of the cavity height.

We note that the first term appearing in front of the square brackets is h_{ppw} [cf. (10)] toward which both (28a) and (28b) would asymptotically converge for $X_s \rightarrow 0$ (i.e., the asymptotic limit of a perfect electric conductor) with the TE-TM PPW modes becoming a degenerate pair. Interestingly, in the air-filled case $\epsilon_r = 1$, (28a) and (28b) take a very compact and advantageous form

$$h_{\text{TE,air}}^{\text{scan}} \simeq \frac{\lambda_0}{2 \cos \theta_{0d}} \left[1 - \frac{1}{\pi} \cot^{-1} \left(\frac{\eta_0 \sec \theta_{0d}}{X_s} \right) \right] \quad (29a)$$

$$h_{\text{TM,air}}^{\text{scan}} \simeq \frac{\lambda_0}{2 \cos \theta_{0d}} \left[1 - \frac{1}{\pi} \cot^{-1} \left(\frac{\eta_0 \cos \theta_{0d}}{X_s} \right) \right]. \quad (29b)$$

We should comment that (28b) and (29b) are less accurate than (28a) and (29a) for a beam approaching endfire, due to the opposite dependence of the argument of the inverse cotangent function with respect to the beam angle: in the TE/TM case, the argument becomes larger/smaller with respect to η_0 [see (27a) and (27b)], and this effect is more pronounced as the PRS reflectivity diminishes (viz., X_s/η_0 increases). Conversely, for a very highly reflective PRS, (28a) and (28b) asymptotically evaluate as

$$h_{\text{TE}}^{\text{scan}} \simeq \frac{\lambda_0}{2\sqrt{\epsilon_r - \sin^2 \theta_{0d}}} \left(1 - \frac{X_s \sqrt{\epsilon_r - \sin^2 \theta_{0d}}}{\pi \eta_0} \right) \quad (30a)$$

$$h_{\text{TM}}^{\text{scan}} \simeq \frac{\lambda_0}{2\sqrt{\epsilon_r - \sin^2 \theta_{0d}}} \left(1 - \frac{X_s \epsilon_r}{\pi \eta_0 \sqrt{\epsilon_r - \sin^2 \theta_{0d}}} \right). \quad (30b)$$

As a side comment, we note that (27a) and (27b) reduce to [29, eq. (32)] for $\hat{\beta} \simeq \hat{\alpha} \rightarrow 0$ which is the condition for having a highly directive broadside beam in either 1-D bidirectional or 2-D LWAs. Indeed, for $\hat{\beta} \simeq \hat{\alpha} \rightarrow 0$, we have $\hat{k}_{z0,\text{op}} \rightarrow 1$ and $\hat{k}_{z0,\text{op}} \rightarrow \sqrt{\epsilon_r}$, thus (27a) and (27b) simplify as

$$h_b = \text{Re} \left\{ \frac{\lambda_0}{2\sqrt{\epsilon_r}} \left[1 - \frac{1}{\pi} \cot^{-1} \left(\frac{\eta_0 / X_s + j}{\sqrt{\epsilon_r}} \right) \right] \right\} \\ \simeq \frac{\lambda_0}{2\sqrt{\epsilon_r}} \left(1 - \frac{X_s \sqrt{\epsilon_r}}{\pi \eta_0} \right) \quad (31)$$

where the last expression is obtained for negligible dielectric losses and a highly reflective PRS (i.e., $X_s \ll \eta_0$). Equation (31) is equivalent to [29, eq. (32)].

Another alternative method that yields analytical formulas for X_s and h can be obtained from (24a) and (24b) under some approximations. The analytical procedure (“Ana.” in Table IV) is a bit lengthy and is thus reported in Appendix B. All the proposed approaches are remarkably accurate as can be inferred from the numerical results reported in Table IV for two typical cases, namely $L = 10\lambda_0$ and $\theta_{0d} = 30^\circ$, and $L = 20\lambda_0$ and $\theta_{0d} = 60^\circ$.

C. Scan Performance

We apply here the considerations and results of the previous Sections IV-A and IV-B to determine the scan performance of a PRS-based 1-D unidirectional LWA, distinguishing between the TE and TM cases. As commented in Section III-A, if one is interested in the scan performance in terms of the gain at the desired scan angle, the TE/TM distinction is not that important: (13)–(18) are accurate enough for evaluating the FBW and the corresponding angular range over which the gain at the desired scan angle does not decay below -3 dB. Conversely, if one is interested in the scan performance in terms of the peak gain as the beam scans, the different dispersive properties of TE and TM leaky modes in PRS-based LWAs discussed in Section IV-A play a key role.

The different behavior of the peak gain over a finite angular range is manifest from Fig. 5(a) to (b), where (a) the TE case and (b) the TM case are shown for a PRS-based unidirectional LWA of length $L = 10\lambda_0$ optimized for radiation at different angles, using the design equations derived in Section IV-B. These results have been obtained by solving numerically the TE and TM dispersion equations, viz., (24a) and (24b), with the optimum design parameters reported in Table III to get the accurate dispersion curves (not shown for brevity) and then evaluating the peak gain either numerically (solid lines) or analytically through (7) (dashed lines). In all cases, the peak gain has been evaluated over a frequency range spanning from $0.6f_0$ to $1.8f_0$ (as highlighted by the green triangles in Fig. 5(a) and (b) for the $\theta_{0d} = 60^\circ$ case only) and then mapped into an angular range by means of the numerical wavenumber dispersion curve and exploiting the relation $\theta_0 = \arcsin \hat{\beta}$.

As can be inferred from Fig. 5(a), in the TE case, the peak gain drops below -3 dB over a finite angular range which is about 40° , 35° , 25° for $\theta_{0d} = 30^\circ$, 45° , 60° , respectively, whereas it remains almost constant for $f > f_0$ in the TM case [see Fig. 5(b)]. This different behavior is readily explained if one looks at (22a) and (22b). Indeed, the variation of $\hat{\beta}$ with frequency is almost the same [12, see Fig. 4]), and in turn that of $\hat{\alpha}$ differs a lot from the TE and TM cases. In particular, it is seen that the frequency variation of $\hat{\alpha}$ in the TE case is way more pronounced than that in the TM case. Since the gain weakly depends on $\hat{\beta}$ but strongly depends on $\hat{\alpha}$, the scan performance is heavily affected in the TE case, and only slightly affected in the TM case. It is interesting to note that a TM-polarized LWA that has its gain optimized at a particular design scan angle will continue to exhibit a beam with a fairly high gain as the beam is frequency-scanned, whereas for the TE case, the gain drops more rapidly as the beam is scanned away from the design scan angle.

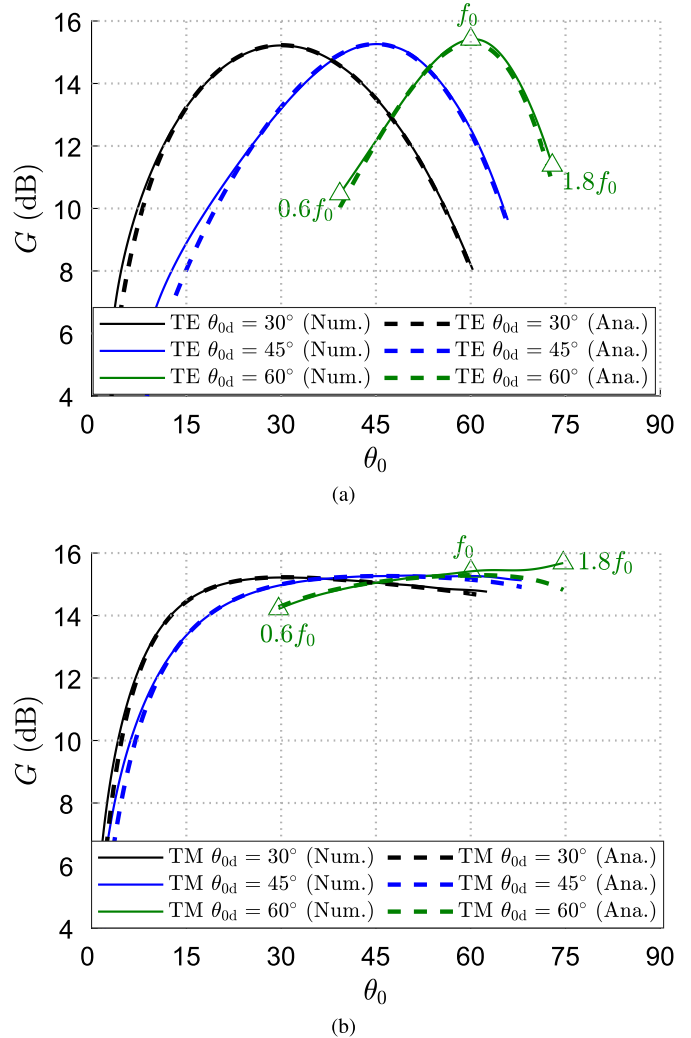


Fig. 5. Peak gain (in dB) versus the scan angle θ_0 for three different PRS-based 1-D unidirectional LWAs optimized for (a) TE polarization and (b) TM polarization and radiating at 30° , 45° , 60° , with an antenna length of $10\lambda_0$. Numerical (analytical) results in solid (dashed) lines. All curves are evaluated over the frequency range $0.6f_0$ – $1.8f_0$ as shown by the triangles for the case $\theta_{0d} = 60^\circ$.

V. NUMERICAL VALIDATION AND APPLICATION EXAMPLE

In this Section V, we want to show how the overall optimization workflow (i.e., Sections III and IV) can be applied to the practical case of a PRS-based 1-D unidirectional LWA. Section V has two main objectives that will be addressed in Sections V-A and V-B, respectively. In Section V-A, we assess the accuracy of the formulas for both the bandwidth performance (results of Section III) and the optimum design rules (results of Section IV) through full-wave simulations of an ideal structure. By ideal structure, we mean a full-wave model with some simplifying hypotheses so as to have an excellent agreement with the theoretical electromagnetic model used in this work. In Section V-B, we demonstrate that the ideal model used in Section V-A is in very good agreement with a more realistic structure, which accounts for both the nonidealities of the PRS (which is no longer modeled with a sheet impedance, but is instead geometrically designed) and the finite size of the ground plane.

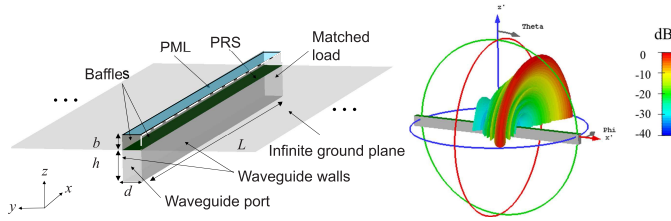


Fig. 6. (a) Ideal electromagnetic model of the PRS-based 1-D unidirectional LWA as implemented in CST Microwave Studio. (b) Three-dimensional view of the radiated pattern normalized to its beam peak.

For the cases analyzed in Sections V-A and V-B we consider, for the sake of simplicity, an air-filled $\epsilon_r = 1$ PPW-like structure of length $L = 10\lambda_0$ operating at the design frequency $f_0 = 10$ GHz, where the PRS consists of an array of inductive metallic strips of width w with period $p \ll \lambda_0$ under TE polarization. This last assumption is advantageous for the PRS modeling since the sheet impedance of an array of inductive ($w \ll p$) metallic strips in free space and under TE polarization is not spatially dispersive, and thus the PRS shows the same Z_s for any β ; the same feature holds for capacitive strips under TM polarization, according to Babinet's principle [36].

In addition, we assume the frequency dispersion of the PRS as $Z_s = j2\pi fL$, where $L = X_s(f_0)/(2\pi f_0)$ to model the inductive behavior of the narrow strips. Although the bandwidth analysis in Section III ignores the frequency dispersion of the PRS, this aspect has negligible effects on the leaky wavenumber dispersion (see [14]), as confirmed by the numerical results of Sections V-A and V-B. It is worthwhile to stress that we only show here one application example, but many other cases have been considered and tested. Specifically, we tested our results for both the TE and the TM cases, for both the inductive and capacitive cases, and for scan angles higher and lower than 30° , for antenna lengths larger or smaller than $L = 10\lambda_0$. Comparison between the results obtained in these different operating conditions confirmed the theoretical LWA performance commented on in Section III-B (the results obtained in terms of FBW, G , and FoM were all in good agreement with those reported in Table III). In all cases, the agreement between the theoretical and full-wave results was comparable with that reported for the application example discussed in Sections V-A and V-B.

A. Ideal Model

The ideal model of the optimized structure designed in CST Microwave Studio [37] and the simulated 3-D radiation pattern (normalized to its beam peak) are shown in Fig. 6(a) and (b), respectively. As shown, the structure is excited at one end with a waveguide port operating in its fundamental TE₁₀ mode (in the coordinate system shown, the subscripts 1 and 0 denote field variation in the z - and y -directions, respectively) and terminated in a matched load (through the definition of another waveguide port with no excitation). A sheet impedance boundary condition is applied on top of the waveguide to represent the PRS. In order to simulate an infinite ground plane, PEC walls are applied to the lateral boundaries of the domain of evaluation. These PEC walls extend along the z -axis with respect to the cavity height to form a 'baffle' on top of which

is put a perfectly matched layer (PML) boundary condition to simulate an electromagnetic environment that matches as much as possible the transverse equivalent network in Fig. 4. The length of the baffle b is set to $b = \lambda_0/4 = 7.5$ mm, whereas the short side of the waveguide d is set to $d = \lambda_0/3 = 10$ mm to have the antenna operating with a single mode at the frequencies of interest. The other relevant parameters, that is, the cavity height and the PRS sheet reactance are set to $h = 0.935h_{ppw} = 16.183$ mm and $X_s = 93.2\Omega$ to have maximum gain at $\theta_{0d} = 30^\circ$ with $L = 10\lambda_0$, according to the results in Table III. These settings yielded an excellent agreement with the theoretical prediction as can be inferred from the 3-D radiation pattern shown in Fig. 6(b), and as we will discuss in detail below.

The first result that shows the impressive correspondence between the ideal model implemented in CST and the theoretical prediction is the comparison between the wavenumber dispersion as calculated numerically from the dispersion equation in (24a) [black solid line in Fig. 7(a)] and as retrieved from the scan angle of the radiation pattern in CST [blue circles in Fig. 7(a)]. In Fig. 7(a), we have also shown the wavenumber dispersion of the equivalent lossy PPW model, that is, (9) [green dashed line in Fig. 7(a)], and of the lossless PPW model, that is, (11) [red dotted line in Fig. 7(a)]. The normalized attenuation constant curves are available only for the lossy PPW model and the numerical results, and the small deviations between them are merely attributed to the frequency dispersion of the PRS constant C in the TE case (commented in Section IV-A) which is not accounted for in the lossy PPW model. For the PPW solution the value of the effective loss tangent was chosen based on a fixed value of C^{TE} , chosen at the desired scan angle of 30° , corresponding to $f = f_0$. The normalized phase constant curves are instead mostly overlapped in all cases. We should note that the excellent agreement between the lossless PPW model dispersion curve and the full-wave results is essential for the accuracy of the formulas provided in Section III to determine the bandwidth performance.

In this regard, we have reported in Fig. 7(b), the variation of the gain at 30° as the frequency changes from 9 to 11 GHz. The gain at 30° , as evaluated from CST, reaches its maximum at 10 GHz (highlighted with a solid green dot) as predicted from theory, and drops off -3 dB over an FBW (the band edges are highlighted with green dashed lines) of around 6.34%. The theoretical prediction (i.e., using (7) for the gain, and (15) for the FBW) and numerical prediction [i.e., through the numerical evaluation of the gain from the radiation pattern in (1) and its corresponding -3 dB frequency points using the numerical wavenumber dispersion reported in Fig. 7(a)] report instead bandwidths of 6.23% and 6.24%, respectively (the band edges are highlighted with black and red dashed lines, respectively, and the peaks are denoted with a black square and a red cross), thus confirming the remarkable accuracy of both the formulas and the model. (The black, red, and green vertical and horizontal dashed lines are almost superimposed.) On the other hand, the gain peak at 30° is 15.37 dB from CST (green dot), whereas it is around 15.23 and 15.22 dB from theory (black square) and from numerical results (red

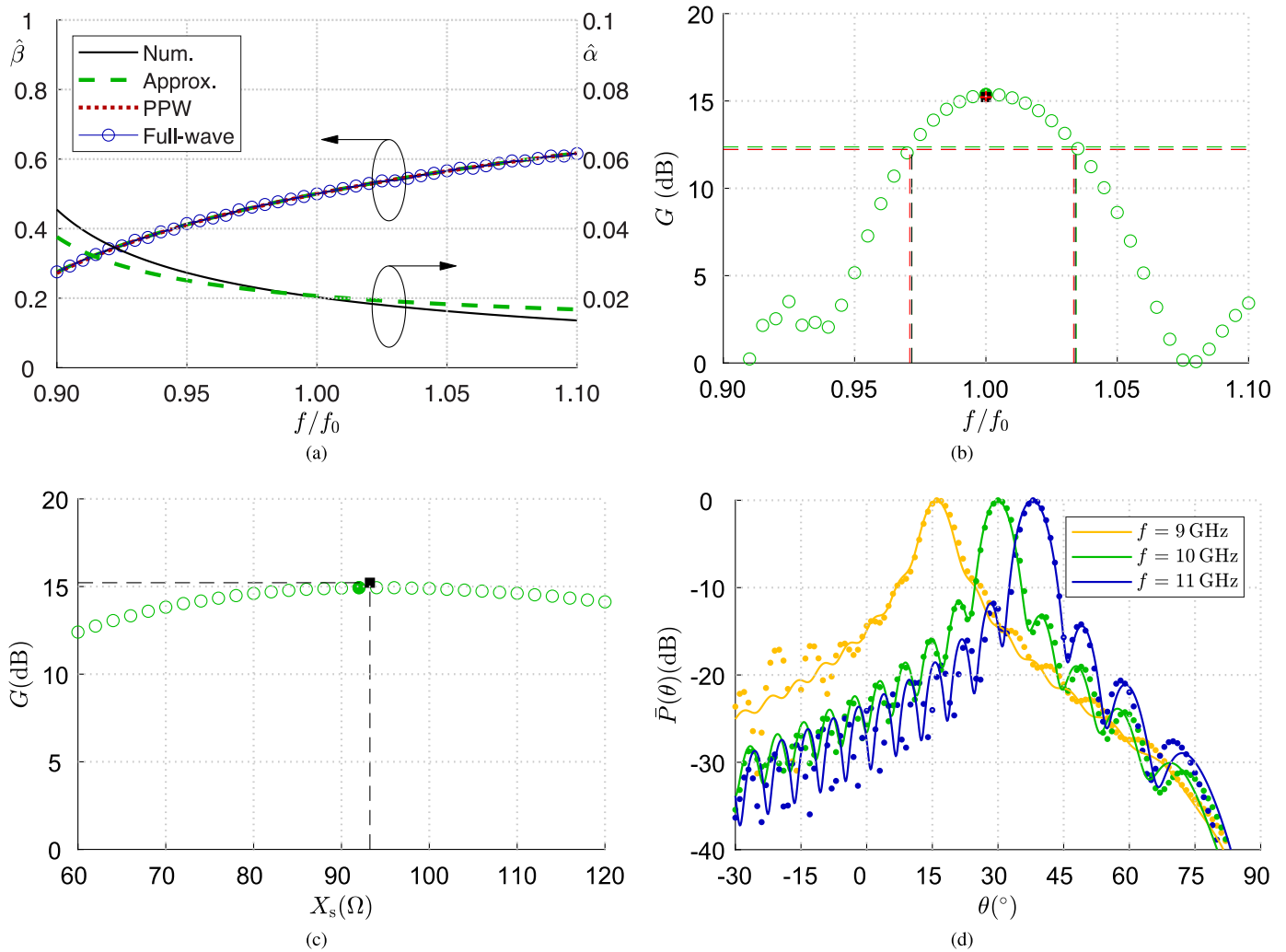


Fig. 7. (a) Dispersion curves $\hat{\beta}$ and $\hat{\alpha}$ versus f/f_0 for the structure investigated in Section V-A (parameters in the text): comparison between different models. (b) Gain (in dB) versus f/f_0 as evaluated with a time-domain simulation of the ideal CST model. The -3 dB frequency points are highlighted with vertical dashed lines. (c) Gain (in dB) versus $X_s(\Omega)$ at $f = 10$ GHz as evaluated with a frequency-domain simulation. The maximum value is highlighted with a green dot, whereas the theoretical prediction is highlighted with a black square. (d) Radiation pattern normalized to its beam peak $\hat{P}(\theta)$ versus θ ($^\circ$) in the principal plane (E-plane) at $f = 9, 10, 11$ GHz (theoretical and full-wave results are reported in solid lines and dots, respectively).

plus sign), respectively; these values lead to FoMs of 2.156, 2.071, and 2.075, for CST, theoretical, and numerical results, respectively.

The previous results were obtained through the time-domain solver of CST in order to get a sufficient number of frequency points over the bandwidth 9–11 GHz with a fast broadband simulation. However, in order to further assess the consistency of our optimum design rules, we decided to use the frequency-domain solver of CST to run a parametric analysis of the structure at a fixed frequency, by varying the value of the reactance sheet X_s from 60Ω to 120 in steps of 2Ω . The result is shown in Fig. 7(c) and demonstrates that the gain is indeed maximized for a value very close to the theoretical one. More precisely, CST obtained a maximum gain of 14.94 dB for 92Ω (green dot) instead of the predicted 15.22 dB for 93.2Ω (black square and dashed lines).

To complete the picture, in Fig. 7(d), the radiation pattern normalized to its beam peak $\hat{P}(\theta) = P(\theta)/P(\theta_0)$ over the principal plane (i.e., $\phi = 0^\circ$) at the center frequency (in green) and at 9 and 11 GHz (in yellow and blue for the lower

and higher edge, respectively) obtained with CST (colored dots) are compared with those obtained with a straightforward implementation of (1) (note that a $\cos^2(\theta)$ has been included to account for polarization effects) together with the numerical wavenumber dispersion reported in Fig. 7(a), showing again an excellent agreement.

B. Realistic Model

The results of Section V-A assessed the accuracy of the proposed formulas when an ideal electromagnetic model of the optimized LWA is designed in CST. Here, we want to remove some simplifying assumptions and show that the proposed optimum design rules still work even for a more realistic structure. Specifically, we refer to the structure depicted in Fig. 8(a), where: 1) an MSG (the relevant design parameters are provided next) replaces the sheet impedance boundary condition; 2) a finite ground plane of lateral size W now appears at both sides of the PRS; and 3) the baffle with the PML on top and the lateral PEC boundary conditions are replaced by radiation boundary conditions. The 3-D radiation pattern of

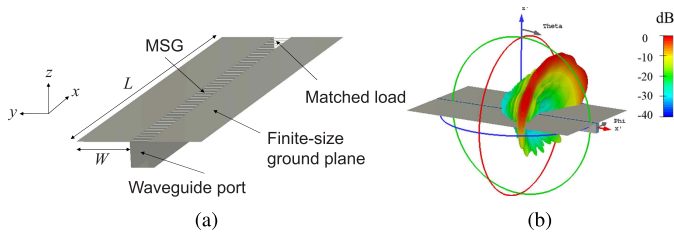


Fig. 8. (a) Realistic electromagnetic model of the PRS-based 1-D unidirectional LWA as implemented in CST Microwave Studio. (b) Three-dimensional view of the radiated pattern normalized to its beam peak.

this realistic structure is shown in Fig. 8(b) and differs from that of the ideal model [cf. Fig. 8(a)] due to the presence of some spurious radiation below the horizon (due to the finite size of the ground plane) and the presence of some ripples along the cone of radiation (due to edge diffraction from the finite-size ground plane). The slight differences between these patterns are commented on in more detail below, by showing the effect that each assumption made in the ideal model has on the radiation performance.

For this purpose, the radiation patterns (normalized to their beam peak) over the principal plane are shown in Fig. 9 for different simulated structures. Specifically, we first reported for comparison purposes only the patterns of the ideal model in Fig. 6(a) (green solid line with dots). Then, we removed the PEC lateral boundary conditions and introduced a ground plane with different sizes W ranging from $2\lambda_0$ and $5\lambda_0$ (see dashed gray lines) for the model in Fig. 8(a). The PRS was represented by a sheet impedance. It is seen that the size of the ground plane has no significant effects on the radiation pattern but in all cases the beam peak shifts to 31° (this is better appreciated from the inset of Fig. 9). However, we found that the finite ground plane is not responsible for the beam peak shift; it is rather the absence of the baffle on top of the PRS. As a matter of fact, when we simulated the structure with a finite size ground plane with $W = 3\lambda_0$ and a baffle extending $b = \lambda_0/4 = 7.5$ mm beyond the PRS and with a PML right on top, we obtained a radiation pattern that points again at exactly 30° (see the yellow solid line with dots).

It is worthwhile to stress here that a strong truncation of the antenna length L may cause an appreciable beam peak shift due to the element pattern, as exhaustively discussed in [38]. However, the optimum gain conditions always lead to radiation efficiencies as high as 92% (see [7, Table II]) for which these effects can safely be neglected for practical antenna lengths (as can be inferred from [38, Fig. 2]) and are thus not discussed further.

Finally, we replaced the sheet impedance boundary condition with an MSG with $p = \lambda_0/4 = 7.5$ mm and $w = 1.82$ mm. Such an MSG shows a reactance sheet of about 93.13Ω (note that the optimum value of X_s is 93.2Ω ; cf. Table III) according to the homogenization formula for inductive metallic strips under TE polarization [26], [27] that we report here for the reader's convenience as

$$X_s = \eta_0 \frac{p}{\lambda_0} \ln \left[\csc \left(\frac{\pi w}{2p} \right) \right]. \quad (32)$$

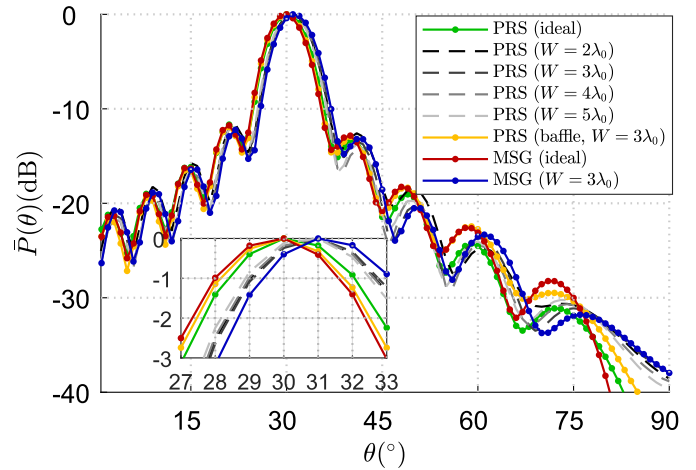


Fig. 9. Radiation patterns normalized to the beam peak $\tilde{P}(\theta)$ versus θ ($^\circ$) in the principal plane at $f = 10$ GHz for different CST models, progressively moving from the ideal one (in green) to the more realistic one (in red). The inset highlights the region close to the beam peak.

Results with the actual MSG but the baffle present [to better match with the ideal model of Fig. 6(a)] are shown with a red dotted line.

As manifest from Fig. 9, there are negligible differences between the ideal model with the MSG (red solid line with dots) and that with the PRS impedance (green solid line with dots). As expected, when we use a finite-size ground plane with $W = 3\lambda_0$ and the MSG, the beam peak shifts again to 31° (see the inset of Fig. 9) because of the absence of the baffle. Except for this small difference, the agreement between all the models is excellent.

For the sake of brevity, we did not repeat all the simulations we showed for the ideal model, since the gain evaluation is a consequence of the radiation pattern that we just showed is in very good agreement among all models. Notwithstanding, we evaluated with full-wave simulations both the gain and the bandwidth performance for the realistic model in Section V-B obtaining results consistent with those shown in Fig. 9 and thus not reported.

VI. CONCLUSION

In a previous work [7], we laid the groundwork to derive by analytical and numerical means optimum conditions for maximizing the gain of 1-D unidirectional LWAs assuming that the leaky normalized phase $\hat{\beta}$ and attenuation $\hat{\alpha}$ constant can be varied freely. In this work, we specialized these results to PRS-based 1-D unidirectional LWAs. For this class of structures, an approximate analytical wavenumber dispersion exists, from which it has been possible to determine the bandwidth performance and the gain–bandwidth FoM when the antenna is designed to operate under the maximum gain conditions described in [7]. In this case, $\hat{\beta}$ and $\hat{\alpha}$ can no longer be varied freely but must obey the hyperbolic relation $C = \hat{\beta}\hat{\alpha}$, where C is the PRS constant. Interestingly, we found that the $\hat{\beta}\hat{\alpha}$ product does not always remain constant; this relation holds approximately true only for TM leaky modes, whereas for TE leaky modes, there exists a strong dependence on the scan angle.

One of the main objectives of this work was to link the *general* optimization procedure described in [7] to a more specific one, providing practical design rules for the general class of PRS-based 1-D unidirectional LWAs. In particular, we were interested in finding the optimum PRS and cavity height parameters that lead to the optimum gain. These design rules have been found with both accurate numerical methods and approximate analytical formulas using a rigorous dispersion analysis of the transverse equivalent network of the structure. Interestingly, we found that there exist indeed four different equivalent ways to maximize the gain for a given antenna length and beam angle, depending on whether an inductive/capacitive PRS and a TE/TM leaky mode are considered.

We should also stress again that, as opposed to PRS-based 1-D bidirectional LWAs [16], PRS-based 1-D unidirectional LWAs are rarely used to radiate a beam at broadside, and the gain–bandwidth FoM depends on the design scan angle, increasing with the design scan angle. The FoM also decreases slightly as the aperture length increases but is almost independent of the aperture length for larger lengths. This is another important finding of this work.

The entire design flow, that is, from the determination of the optimum $\hat{\beta}$ and $\hat{\alpha}$ to the determination of the optimum design parameters, has been demonstrated for the reference case of an air-filled PPW-like structure of length $L = 10\lambda_0$ at 10 GHz excited in its TE fundamental leaky mode, when the PRS is a metal strip grating. The radiating performance of this structure has been optimized for achieving maximum gain when the beam angle is fixed and was validated through time-domain and frequency-domain CST full-wave simulations, as well as an accurate numerical leaky-wave analysis. Two CST models have been implemented: an ideal model that better matches the theory, and a realistic model that better matches a practical realization of the structure. A remarkable agreement was found among all techniques, thus corroborating the validity and accuracy of the proposed analysis for the optimization of the radiating properties of finite-size 1-D unidirectional LWAs. Future activities are planned to derive similar optimum conditions for the relevant cases of finite-size 1-D periodic and 1-D bidirectional LWAs.

APPENDIX A

EXTENSION TO THE THICK PRS CASE

To have a more compact notation, the results of this appendix are expressed in terms of the normalized sheet (input) admittance defined as $\tilde{Y}_s = \eta_0/Z_s$ ($\tilde{Y}_{in} = \eta_0/Z_{in}$).

The extension to the *thick* PRS case requires modifications to the formulas for the PRS constant, that is, (23) and for the cavity height, that is, (24a) and (24b). We start from the modification required by (23). As shown in [19] and [20], for a *thick* PRS, the normalized input admittance looking upward \tilde{Y}_{in}^+ is what is important. For a lossy, thin PRS, \tilde{Y}_{in}^+ is related to \tilde{Y}_s through

$$\tilde{Y}_{in}^+ = \tilde{G}_{in}^+ + j\tilde{B}_{in}^+ = 1 + \tilde{G}_s + j\tilde{B}_s. \quad (33)$$

The relation between the PRS constant C_b and the reactance of a lossless, thin PRS [viz., (23)] has been extended to the

lossy case in [11] and reads

$$C_b = \frac{\epsilon_r}{2} \left(\tan \delta + \frac{2\sqrt{\epsilon_r}}{\pi} \frac{1 + \tilde{G}_s}{(1 + \tilde{G}_s)^2 + \tilde{B}_s^2} \right). \quad (34)$$

Hence, (34) is easily generalized to the thick PRS case upon making the following substitutions:

$$\begin{cases} 1 + \tilde{G}_s \rightarrow \tilde{G}_{in}^+ \\ \tilde{B}_s \rightarrow \tilde{B}_{in}^+ \end{cases}. \quad (35)$$

As concerns the cavity height formulas, we have a reactance term X_s appearing in (24a) and (24b) that we need to generalize. To this aim, we first need to distinguish between the TE and TM cases. For the TE case, a more general form reads

$$\tilde{G}_{in}^+ + j\tilde{B}_{in}^+ - j\hat{k}_{zd} \cot(2\pi\hat{k}_{zd}h/\lambda) = 0 \quad (36)$$

whereas for the TM case reads

$$\tilde{G}_{in}^+ + j\tilde{B}_{in}^+ - j\epsilon_r\hat{k}_{zd}^{-1} \cot(2\pi\hat{k}_{zd}h/\lambda) = 0. \quad (37)$$

Comparison between (36) and (24a) reveals that the sought generalization requires, in the TE case, the following substitutions:

$$\begin{cases} \hat{k}_{zd} \rightarrow \tilde{G}_{in}^+ \\ \tilde{X}_s \rightarrow \tilde{B}_{in}^+ \end{cases}. \quad (38)$$

By the same token, comparison between (37) and (24b) provides, in the TM case, the following substitutions:

$$\begin{cases} \hat{k}_{zd} \rightarrow 1/\tilde{G}_{in}^+ \\ \tilde{X}_s \rightarrow -1/\tilde{B}_{in}^+ \end{cases}. \quad (39)$$

APPENDIX B

ACCURATE FORMULAS FOR CAVITY HEIGHT AND PRS REACTANCE SHEET

We aim at deriving approximate closed-form expressions for the cavity height h and the PRS sheet reactance X_s once the $\hat{\beta}$ and $\hat{\alpha}$ of the TE or TM dominant leaky wave propagating in a PRS-based 1-D unidirectional LWA are given *a priori* at a given operating frequency.

To this aim, we start from (24a) and (24b) and note that if we assume the PRS to be sufficiently reflective, that is, $X_s \ll \eta_0$, the optimum cavity height h_{opt} should be designed close to the first resonance, that is, $2\pi\hat{k}_{zd}h/\lambda \simeq \pi$, so we use the first-order Laurent approximation for the cotangent function, viz., $\cot(z) \simeq 1/(z - \pi)$. Under this assumption, simple but lengthy algebraic manipulations allow for having a closed-form expression for h_{opt} in terms of $\hat{\beta}$ and $\hat{\alpha}$, solely, and for $\tilde{B}_s = -\eta_0/X_s$ in terms of $\hat{\beta}$ and $\hat{\alpha}$, and h_{opt} .

We show here the whole derivation for the TE case (the TM case follows straightforward and is thus not repeated; only final results are provided). Therefore, from (24a) we have

$$\tilde{B}_s^{TE} \simeq j\hat{k}_{zd} + \frac{\hat{k}_{zd}}{k_0\hat{k}_{zd}h}. \quad (40)$$

For the sake of simplicity, we define

$$\tilde{B}_{s1}^{TE} \equiv j\hat{k}_{zd} \quad \tilde{B}_{s2}^{TE} \equiv \frac{\hat{k}_{zd}}{k_0\hat{k}_{zd}h - \pi} \quad (41)$$

such that $\tilde{B}_s^{\text{TE}} = \tilde{B}_{s1}^{\text{TE}} + \tilde{B}_{s2}^{\text{TE}}$. From (40) and the definitions (41), $\tilde{B}_{s,\text{opt}}^{\text{TE}}$ and $h_{\text{opt}}^{\text{TE}}$ are expressed by the following equations:

$$\tilde{B}_{s,\text{opt}}^{\text{TE}} = \text{Re}[\tilde{B}_{s1}^{\text{TE}}] + \text{Re}[\tilde{B}_{s2}^{\text{TE}}] \quad (42)$$

$$h_{\text{opt}}^{\text{TE}}; \quad \text{Im}[\tilde{B}_{s1}^{\text{TE}}] + \text{Im}[\tilde{B}_{s2}^{\text{TE}}] = 0. \quad (43)$$

After simple algebraic manipulations, we obtain the following expressions for the real and imaginary parts of $\tilde{B}_{s1,2}^{\text{TE}}$:

$$\begin{aligned} \text{Re}[\tilde{B}_{s1}^{\text{TE}}] &= \hat{\alpha}_{z0} \\ \text{Re}[\tilde{B}_{s2}^{\text{TE}}] &= \frac{k_0 h (\hat{\beta}_{zd}^2 + \hat{\alpha}_{zd}^2) - \hat{\beta}_{zd} h}{(k_0 h \hat{\beta}_{zd} - \pi)^2 + (k_0 h \hat{\alpha}_{zd})^2} \\ \text{Im}[\tilde{B}_{s1}^{\text{TE}}] &= \hat{\beta}_{z0} \\ \text{Im}[\tilde{B}_{s2}^{\text{TE}}] &= \frac{\pi \hat{\alpha}_{zd}}{(k_0 h \hat{\beta}_{zd} - \pi)^2 + (k_0 h \hat{\alpha}_{zd})^2}. \end{aligned} \quad (44)$$

Putting all the pieces together, we get an equation for $\tilde{B}_{s,\text{opt}}^{\text{TE}}$ in terms of h , which reads

$$\tilde{B}_{s,\text{opt}}^{\text{TE}} = \hat{\alpha}_{z0} - \frac{\hat{\beta}_{z0} \pi - k_0 h |\hat{k}_{zd}|^2}{(k_0 h \hat{\beta}_{zd} - \pi)^2 + (k_0 h \hat{\alpha}_{zd})^2} \quad (45)$$

and a second-order polynomial equation $a_2 x^2 + a_1 x + a_0 = 0$ for $x = h_{s,\text{opt}}^{\text{TE}}$ with the following coefficients:

$$\begin{cases} a_2 = k_0^2 |\hat{k}_{zd}|^4 \\ a_1 = -2k_0 \pi \hat{\beta}_{z0} \\ a_0 = \pi^2 [1 + \hat{\alpha}_{z0}/(\hat{\beta}_{z0} \pi)]. \end{cases} \quad (46)$$

Plugging the two roots of $h_{\text{opt}}^{\text{TE}}$ into (45), we obtain a capacitive ($\tilde{B}_s > 0$) and an inductive solution ($\tilde{B}_s < 0$) for $\tilde{B}_{s,\text{opt}}^{\text{TE}}$.

With similar steps, the following results are found in the TM case. The reactance sheet is given by

$$\begin{aligned} \tilde{B}_{s,\text{opt}}^{\text{TM}} &= -\frac{\hat{\alpha}_{z0}}{|\hat{k}_{z0}|^2} \\ &+ \frac{\varepsilon_r [k_0 h (\hat{\beta}_{zd}^2 - \hat{\alpha}_{zd}^2) - \hat{\beta}_{zd} \pi]}{[k_0 h (\hat{\beta}_{zd}^2 - \hat{\alpha}_{zd}^2) - \hat{\beta}_{zd} \pi]^2 + [2k_0 h \hat{\beta}_{zd} \hat{\alpha}_{zd} - \hat{\alpha}_{zd} \pi]^2} \end{aligned} \quad (47)$$

whereas $h_{s,\text{opt}}^{\text{TM}}$ is given by a second-order polynomial equation $b_2 x^2 + b_1 x + b_0 = 0$ for $x = h_{s,\text{opt}}^{\text{TM}}$ with the following coefficients:

$$\begin{cases} b_2 = k_0^2 |\hat{k}_{zd}|^4 \\ b_1 = -2k_0 \pi \hat{\beta}_{z0} [|\hat{k}_{zd}|^2 - \varepsilon_r \hat{\alpha}_{z0} |\hat{k}_{z0}|^2 / (\hat{\beta}_{z0} \pi)] \\ b_0 = \pi^2 [|\hat{k}_{zd}|^2 - \varepsilon_r \hat{\alpha}_{z0} |\hat{k}_{z0}|^2 / (\hat{\beta}_{z0} \pi)]. \end{cases} \quad (48)$$

REFERENCES

- [1] D. R. Jackson, C. Caloz, and T. Itoh, "Leaky-wave antennas," *Proc. IEEE*, vol. 100, no. 7, pp. 2194–2206, Jul. 2012.
- [2] F. Monticone and A. Alù, "Leaky-wave theory, techniques, and applications: From microwaves to visible frequencies," *Proc. IEEE*, vol. 103, no. 5, pp. 793–821, May 2015.
- [3] S. Campione, C. Guclu, Q. Song, O. Boyraz, and F. Capolino, "An optical leaky wave antenna with Si perturbations inside a resonator for enhanced optical control of the radiation," *Opt. Express*, vol. 20, no. 19, pp. 21305–21317, 2012.
- [4] W. Fuscaldo *et al.*, "Systematic design of THz leaky-wave antennas based on homogenized metasurfaces," *IEEE Trans. Antennas Propag.*, vol. 66, no. 3, pp. 1169–1178, Mar. 2018.
- [5] A. Goudarzi, M. M. Honari, and R. Mirzavand, "A high-gain leaky-wave antenna using resonant cavity structure with unidirectional frequency scanning capability for 5G applications," *IEEE Access*, vol. 9, pp. 138858–138865, 2021.
- [6] M. Memarian and G. V. Eleftheriades, "Dirac leaky-wave antennas for continuous beam scanning from photonic crystals," *Nature Commun.*, vol. 6, no. 1, pp. 1–9, May 2015.
- [7] W. Fuscaldo, A. Galli, and D. R. Jackson, "Optimization of the radiating features of 1-D unidirectional leaky-wave antennas," *IEEE Trans. Antennas Propag.*, vol. 70, no. 1, pp. 111–125, Jan. 2022.
- [8] D. R. Jackson and A. A. Oliner, "A leaky-wave analysis of the high-gain printed antenna configuration," *IEEE Trans. Antennas Propag.*, vol. AP-36, no. 7, pp. 905–910, Jul. 1988.
- [9] D. R. Jackson, A. A. Oliner, and A. Ip, "Leaky-wave propagation and radiation for a narrow-beam multiple-layer dielectric structure," *IEEE Trans. Antennas Propag.*, vol. 41, no. 3, pp. 344–348, Mar. 1993.
- [10] T. Zhao, D. R. Jackson, J. T. Williams, and A. A. Oliner, "Simple CAD model for a dielectric leaky-wave antenna," *IEEE Antennas Wireless Propag. Lett.*, vol. 3, pp. 243–245, 2004.
- [11] W. Fuscaldo, "Rigorous evaluation of losses in uniform leaky-wave antennas," *IEEE Trans. Antennas Propag.*, vol. 68, no. 2, pp. 643–655, Feb. 2020.
- [12] W. Fuscaldo, P. Burghignoli, and A. Galli, "The transition between reactive and radiative regimes for leaky modes in planar waveguides based on homogenized partially reflecting surfaces," *IEEE Trans. Microw. Theory Techn.*, vol. 68, no. 12, pp. 5259–5269, Dec. 2020.
- [13] G. Lovat, P. Burghignoli, and D. R. Jackson, "Fundamental properties and optimization of broadside radiation from uniform leaky-wave antennas," *IEEE Trans. Antennas Propag.*, vol. 54, no. 5, pp. 1442–1452, May 2006.
- [14] G. Lovat, P. Burghignoli, F. Capolino, and D. R. Jackson, "Bandwidth analysis of highly-directive planar radiators based on partially-reflecting surfaces," in *Proc. 1st Eur. Conf. Antennas Propag.*, Nov. 2006, pp. 1–6.
- [15] A. Sutinjo, M. Okoniewski, and R. H. Johnston, "Beam-splitting condition in a broadside symmetric leaky-wave antenna of finite length," *IEEE Antennas Wireless Propag. Lett.*, vol. 7, pp. 609–612, 2008.
- [16] D. R. Jackson *et al.*, "The fundamental physics of directive beaming at microwave and optical frequencies and the role of leaky waves," *Proc. IEEE*, vol. 99, no. 10, pp. 1780–1805, Oct. 2011.
- [17] S. A. Hosseini, F. Capolino, and F. De Flaviis, "A new formula for the pattern bandwidth of Fabry-Pérot cavity antennas covered by thin frequency selective surfaces," *IEEE Trans. Antennas Propag.*, vol. 59, no. 7, pp. 2724–2727, Jul. 2011.
- [18] A. Hosseini, F. Capolino, F. De Flaviis, P. Burghignoli, G. Lovat, and D. R. Jackson, "Improved bandwidth formulas for Fabry-Pérot cavity antennas formed by using a thin partially-reflective surface," *IEEE Trans. Antennas Propag.*, vol. 62, no. 5, pp. 2361–2367, May 2014.
- [19] A. Hosseini, F. De Flaviis, and F. Capolino, "Design formulas for planar Fabry-Pérot cavity antennas formed by thick partially reflective surfaces," *IEEE Trans. Antennas Propag.*, vol. 64, no. 12, pp. 5487–5491, Dec. 2016.
- [20] A. T. Almutawa, A. Hosseini, D. R. Jackson, and F. Capolino, "Leaky-wave analysis of wideband planar Fabry-Pérot cavity antennas formed by a thick PRS," *IEEE Trans. Antennas Propag.*, vol. 67, no. 8, pp. 5163–5175, Aug. 2019.
- [21] Y.-F. Lu and Y.-C. Lin, "A hybrid approach for finite-size Fabry-Pérot antenna design with fast and accurate estimation on directivity and aperture efficiency," *IEEE Trans. Antennas Propag.*, vol. 61, no. 11, pp. 5395–5401, Nov. 2013.
- [22] W. Fuscaldo, D. R. Jackson, and A. Galli, "A general and accurate formula for the beamwidth of 1-D leaky-wave antennas," *IEEE Trans. Antennas Propag.*, vol. 65, no. 4, pp. 1670–1679, Apr. 2017.
- [23] V. Galdi and I. M. Pinto, "A simple algorithm for accurate location of leaky-wave poles for grounded inhomogeneous dielectric slabs," *Microw. Opt. Technol. Lett.*, vol. 24, no. 2, pp. 135–140, Jan. 2000.
- [24] D. R. Jackson and N. G. Alexopoulos, "Gain enhancement methods for printed circuit antennas," *IEEE Trans. Antennas Propag.*, vol. AP-33, no. 9, pp. 976–987, Sep. 1985.
- [25] T. Tamir and A. A. Oliner, "Guided complex waves. Part 2: Relation to radiation patterns," *Proc. Inst. Electr. Eng.*, vol. 110, no. 2, pp. 325–334, 1963.
- [26] S. Tretyakov, *Analytical Modeling in Applied Electromagnetics*. Norwood, MA, USA: Artech House, 2003.
- [27] O. Luukkonen *et al.*, "Simple and accurate analytical model of planar grids and high-impedance surfaces comprising metal strips or patches," *IEEE Trans. Antennas Propag.*, vol. 56, no. 6, pp. 1624–1632, Jun. 2008.

- [28] L. O. Goldstone and A. A. Oliner, "Leaky-wave antennas I: Rectangular waveguides," *IRE Trans. Antennas Propag.*, vol. 7, no. 4, pp. 307–319, Oct. 1959.
- [29] T. Zhao, D. R. Jackson, J. T. Williams, and A. A. Oliner, "General formulas for 2-D leaky-wave antennas," *IEEE Trans. Antennas Propag.*, vol. 53, no. 11, pp. 3525–3533, Nov. 2005.
- [30] R. M. Foster, "A reactance theorem," *Bell Syst. Tech. J.*, vol. 3, no. 2, pp. 259–267, Apr. 1924.
- [31] G. Valerio, D. R. Jackson, and A. Galli, "Fundamental properties of surface waves in lossless stratified structures," *Proc. Roy. Soc. A, Math., Phys. Eng. Sci.*, vol. 466, no. 2120, pp. 2447–2469, Aug. 2010.
- [32] G. Valerio, D. R. Jackson, and A. Galli, "Formulas for the number of surface waves on layered structures," *IEEE Trans. Microw. Theory Techn.*, vol. 58, no. 7, pp. 1786–1795, Jul. 2010.
- [33] O. Luukkonen, M. G. Silveirinha, A. B. Yakovlev, C. R. Simovski, I. S. Nefedov, and S. A. Tretyakov, "Effects of spatial dispersion on reflection from mushroom-type artificial impedance surfaces," *IEEE Trans. Microw. Theory Techn.*, vol. 57, no. 11, pp. 2692–2699, Nov. 2009.
- [34] R. Sorrentino, "Transverse resonance technique," in *Numerical Techniques for Microwave and Millimeter-Wave Passive Structures*, T. Itoh, Ed. New York, NY, USA: Wiley, 1989, ch. 11.
- [35] T. Tamir and A. A. Oliner, "Guided complex waves. Part I: Fields at an interface," *Proc. Inst. Electr. Eng.*, vol. 110, no. 2, pp. 310–324, 1963.
- [36] J. A. Kong, *Electromagnetic Wave Theory*. New York, NY, USA: Wiley, 1986.
- [37] (2019). *CST Products Darmstadt, Germany*. [Online]. Available: <http://www.cst.com>
- [38] M. Schühler, R. Wansch, and M. A. Hein, "On strongly truncated leaky-wave antennas based on periodically loaded transmission lines," *IEEE Trans. Antennas Propag.*, vol. 58, no. 11, pp. 3505–3514, Nov. 2010.



Walter Fuscaldo (Senior Member, IEEE) received the B.Sc. and M.Sc. degrees (*cum laude*) in telecommunications engineering from Sapienza University of Rome, Rome, Italy, in 2010 and 2013, respectively, and the dual Ph.D. degree [(*cum laude*) and with the Doctor Europaeus label] in information and communication technology (applied electromagnetics curriculum) from the Department of Information Engineering, Electronics and Telecommunications (DIET), and the Institut d'Électronique et de Télécommunications de Rennes (IETR), Université de

Rennes 1, Rennes, France, in 2017, under a cotutelle agreement between the institutions.

In 2014, 2017, and 2018, he was a Visiting Researcher with the NATO-STO Center for Maritime Research and Experimentation, La Spezia, Italy. In 2016, he was a Visiting Researcher with the University of Houston, Houston, TX, USA. In July 2017, he was a Post-Doctoral Researcher with the Sapienza University of Rome. In July 2020 he joined the Institute for Microelectronics and Microsystems (IMM), Rome, Italy, as a Researcher of the National Research Council of Italy. His current research interests include propagation of leaky waves, surface waves and plasmonic waves, analysis and design of leaky-wave antennas, generation of localized electromagnetic waves, graphene electromagnetics, metasurfaces, and THz antennas.

Dr. Fuscaldo was awarded several prizes, among which are the prestigious Young Engineer Prize for the Best Paper presented at the 46th European Microwave Conference in 2016 and the Best Paper in Electromagnetics and Antenna Theory at the 12th European Conference on Antennas and Propagation in 2018. He was also awarded for his reviewer activity the Publons Peer Review Awards in Engineering in 2018 and 2019 and in Cross-field in 2019, and the IEEE Reviewer Certificate for excellent performance for the IEEE TRANSACTIONS ON ANTENNAS AND PROPAGATION journal in 2019 and 2020. He is also an Associate Editor of the *IET Microwaves, Antennas and Propagation* journal and *IET Electronic Letters*, and a Topic Editor of *MDPI Crystals* journal.



Alessandro Galli (Member, IEEE) received the Laurea degree in electronics engineering and the Ph.D. degree in applied electromagnetics from the Sapienza University of Rome, Rome, Italy, in 1990 and 1994, respectively.

Since 1990, he has been with the Department of Information Engineering, Electronics and Telecommunications, Sapienza University of Rome. He became an Assistant Professor and an Associate Professor with the Sector of Electromagnetic Fields in 2000 and 2002, respectively. In 2013 he passed the

National Scientific Qualification, and in 2020 he definitively achieved the role of Full Professor in the same sector. He is currently teaching or co-teaching courses on electromagnetic fields, advanced antenna engineering, microwaves, and engineering electromagnetics. He has authored more than 300 articles in international journals, books, and conference proceedings. He holds a patent for an invention of a leaky-wave antenna. His research interests include electromagnetic guided-wave and radiation theory and applications ranging from microwaves to terahertz. Specific topics include leaky waves and leaky-wave antennas, periodic and multilayered printed structures, beam focusing devices, and complex media and metamaterials. His research activities have also included topics in geoelectromagnetics, bioelectromagnetics, and plasma heating.

Prof. Galli was elected as the Italian Representative on the Board of Directors of the European Microwave Association (EuMA) for the 2010–2012 and 2013–2015 triennium. He was the General Co-Chair of the 2014 European Microwave Week, the most important conference event in the electromagnetic area at the European level. Since its foundation in 2012, he has been the Coordinator of the European Courses on Microwaves (EuCoM), and the first European educational institution on microwaves. He is also a member of the leading scientific societies of electromagnetics. He was a recipient of various grants and prizes for his research activity, such as the Barzilai Prize for the best scientific work of under-35 researchers from the 10th National Meeting of Electromagnetics in 1994, and the Quality Presentation Recognition Award of the International Microwave Symposium by the IEEE Microwave Theory and Techniques Society in 1994 and 1995. In 2017, he has been elected as the Best Teacher of the courses of the European School of Antennas (ESoA). He is also an Associate Editor of two international journals on microwaves, antennas, and propagation.



David R. Jackson (Fellow, IEEE) was born in St. Louis, MO, USA, in March 1957. He received the B.S.E.E. and M.S.E.E. degrees from the University of Missouri, Columbia, MO, USA, in 1979 and 1981, respectively, and the Ph.D. degree in electrical engineering from the University of California at Los Angeles, Los Angeles, CA, USA, in 1985.

From 1985 to 1991, he was an Assistant Professor with the Department of Electrical and Computer Engineering, University of Houston, Houston, TX, USA. From 1991 to 1998, he was an Associate

Professor with the Department of Electrical and Computer Engineering. Since 1998, he has been a Professor with the Department of Electrical and Computer Engineering. His research interests include microstrip antennas and circuits, leaky-wave antennas, wave propagation effects, including surface waves and leaky waves, leakage, and radiation effects in microwave integrated circuits, periodic structures, and electromagnetic compatibility and interference.

Dr. Jackson has served as the Chair for USNC-URSI, the U.S. National Committee (USNC) for URSI, the International Union of Radio Science, from 2015 to 2018. He also serves on the IEEE Antennas and Propagation Society (AP-S) Committee on Promoting Equality (COPE) and the Microwave Field Theory (MTT-1) Technical Committee of the Microwave Theory and Techniques Society. Previously, he has been the Chair of the Distinguished Lecturer Committee of the IEEE AP-S, the Transnational Committee of the IEEE AP-S, and the Chapter Activities Committee of the AP-S, a Distinguished Lecturer for the AP-S, and a member of the AdCom for the AP-S. He has also served as the Chair of Commission B of USNC-URSI and the Secretary of this Commission. He also previously served as an Associate Editor for the *Journal Radio Science* and the *International Journal of RF and Microwave Computer-Aided Engineering*. He has been an Associate Editor of the IEEE TRANSACTIONS ON ANTENNAS AND PROPAGATION.